ELSEVIER

Chemical Geology xx (2005) xxx–xxx

CHEMICAL GEOLOGY
INCLUDING
ISOTOPE GEOSCIENCE

www.elsevier.com/locate/chemgeo

Role of lithosphere–asthenosphere interaction in the genesis of Quaternary alkali and tholeiitic basalts from Datong, western North China Craton

Yi-Gang Xu [a,*], Jin-Long Ma [a], Frederick A. Frey [b], Mark D. Feigenson [c], Jiang-Feng Liu [a]

[a] *Key Laboratory of Isotope Geochronology and Geochemistry, Guangzhou Institute of Geochemistry, Chinese Academy of Sciences, 510640 Guangzhou, PR China*

[b] *Department of Earth, Atmospheric and Planetary Sciences, Massachusetts Institute of Technology, Cambridge MA 02139, United States*

[c] *Department of Geological Sciences, Rutgers University, 610 Taylor Road, Piscataway, NJ, 08854, United States*

Received 18 February 2005; received in revised form 9 August 2005; accepted 10 August 2005

Abstract

The geochemistry of Quaternary volcanic rocks from Datong provides important constraints on the petrogenesis of continental alkali and tholeiitic basalts and lithospheric evolution in the western North China Craton. Alkali basalts in north Datong have trace element compositions similar to oceanic island basalts (OIB). They show nearly homogenous isotopic compositions (ε_{Nd} = 5.4–6.8 and $^{87}Sr/^{86}Sr$ = 0.7035–0.7037) that resemble the nearby Hannuoba Miocene basalts, indicating that the two lava suites share a similar asthenospheric source. However, Datong basalts have conspicuously lower Al_2O_3 and CaO, higher SiO_2 and HREE contents and Na/Ti ratios, compared to Hannuoba lavas at comparable MgO. This compositional difference is attributable to the combined effect of source difference and temporal decrease in melting depth. The latter reflects Cenozoic lithospheric thinning of the western North China Craton.

Tholeiitic basalts in southeast Datong have incompatible element ratios that differ from OIB; they have lower ε_{Nd} (1.3–3.7) and higher $^{87}Sr/^{86}Sr$ (0.7039–0.7046) compared to alkali basalts. These moderately evolved rocks (MgO < 7%) display unusually high Cr concentrations (>200 ppm), a nearly flat LREE pattern and a fractionated HREE with the "kink" occurring at Gd. A shallow melting depth (<60 km), suggested by their Q-normative composition, is in conflict with the residual garnet in the source (>75 km) as required by REE modeling. This paradox, which is reminiscent of that for Hawaiian tholeiites, can be reconciled if garnet lherzolite melts react with refractory peridotites during which orthopyroxene is dissolved and olivine precipitates. The diagnostic consequence of this melt–rock reaction includes increases in SiO_2 and Cr, decreases in Al_2O_3 and CaO, and formation of "kinked" REE patterns. Involvement of lithospheric mantle in the genesis of Datong tholeiites may be related to the Cenozoic lithospheric thinning/erosion in the western North China Craton. The spatial distribution of Datong alkali and tholeiitic basalts may be related to enhanced extension along the lithospheric boundary between the Western Block of the North China Craton and the Trans-North China Orogen.

Keywords: Alkali basalt; Tholeiite; Petrogenesis; Geochemistry; Lithospheric thinning; Lithosphere–asthenosphere interaction; Western North China craton

* Corresponding author. Tel.: +86 20 85290109; fax: +86 20 85290130.
E-mail address: yigangxu@gig.ac.cn (Y.-G. Xu).

0009-2541/$ - see front matter © 2005 Elsevier B.V. All rights reserved.
doi:10.1016/j.chemgeo.2005.08.004

1. Introduction

Continental basalts commonly show a wider compositional diversity than oceanic counterparts (Perry et al., 1987; Song et al., 1990; Zhi et al., 1990; Fan and Hooper, 1991; Fitton et al., 1991; Wilson and Downes, 1991; Zhou and Mukasa, 1997; Jung and Masberg, 1998; Zou et al., 2000; Barry et al., 2003). There is ample evidence that the continental lithosphere (crust+mantle) plays a central role in creating this compositional diversity. Continental lithosphere may serve as a passive mechanical barrier to continuous upwelling of the asthenosphere, thereby defining the final depth of melting (e.g., Langmuir et al., 1992; Fram and Lesher, 1993), or it may have a more direct role in determining magma composition by serving as a source component (e.g., Perry et al., 1987; Fitton et al., 1991) or a magma contaminant (e.g., Glazner and Farmer, 1992). These possible roles for continental lithosphere must be evaluated when using the geochemistry of continental basalts to constrain the magma sources and accompanying mantle processes (e.g., Cox and Hawkesworth, 1984; Perry et al., 1987; DePaolo and Daley, 2000). For example, the effect of a thick lithospheric lid on the composition of asthenosphere-derived basalt is indicated by indicators of the mean pressure of melt segregation, such as FeO, SiO_2 and Na/Ti (Langmuir et al., 1992; Putirka, 1999a). The effect of wall-rock contamination during ascent of magmas through lithosphere is especially important for tholeiitic basalt which ascends relatively slowly due to low volatile contents (Cox and Hawkesworth, 1984). Clearly, determining the relative contribution of continental lithospheric mantle (CLM) and crust to basaltic composition is a formidable task for petrologists.

The alkali and tholeiitic basalt in the Quaternary Datong volcanic field in North China provides new information about the relative roles of asthenosphere and lithosphere in the generation of continental basalt. Like many other volcanic terrains, the two rock types from this locality display different geochemical signatures. In addition, the two basalt types show distinct spatial provinciality, rather than intercalation as at Hannuoba, 100 km north of Datong (Zhi et al., 1990; Song et al., 1990). On the other hand, it is well established that the Archaean North China Craton (NCC) experienced widespread thermotectonic reactivations during the Late Mesozoic and Cenozoic, which resulted in replacement of the old, cold, thick and depleted lithospheric mantle by young, hot, thin and fertile mantle (Menzies et al., 1993; Griffin et al., 1998; Xu, 2001). More importantly, the lithospheric thinning in the NCC may have proceeded in a diachronous way. While the lithosphere is progressively thinned in the western NCC (located east to the Daxinganling–Taihangshan gravity lineament, Fig. 1) during the Cenozoic, it is thickened in the eastern NCC, probably related to regional thermal decay following peak magmatism in the Late Cretaceous (Xu et al., 2004a). Datong Quaternary basalts are emplaced in western NCC and are compositionally distinct from Oligocene and Miocene lavas in the region (Xu et al., 2004a). Petrogenetic characterization of Datong lavas is therefore the key to understand the lithosphere–asthenosphere interaction during the dramatic change in lithospheric architecture in the NCC (Menzies et al., 1993; Griffin et al., 1998; Xu, 2001). The objectives of this study are:

(a) to present major, trace element and Sr–Nd isotopic composition of alkali and tholeiitic basalts from Datong and to discuss their petrogenesis with emphasis on defining the role of lithosphere–asthenosphere interaction in continental basaltic volcanism;
(b) to compare geochemical data of the Datong lavas with the well-studied Miocene basalts from Hannuoba, to define the temporal change in mantle melting conditions in the NCC using forward and inverse REE modeling techniques and to test the proposed model on the Cenozoic lithospheric evolution of the NCC; and
(c) to propose a tectonomagmatic model to explain the spatial distribution of the Datong basalts.

2. Geologic background and petrographic characteristics

Traditionally, the NCC is separated into two different tectonic domains by the N–S trending Daxinganling–Taihangshan gravity lineament (DTGL) (Ye et al., 1987; Ma, 1989; Menzies and Xu, 1998). This division was recently refined on the basis of lithological, geochemical and metamorphic *P–T* path data of the basement rocks (Zhao et al., 2001). The basement of the NCC is now divided into three blocks, namely Eastern and Western Blocks and the intervening Trans-North China Orogen (Fig. 1a). The Eastern Block consists predominantly of Early to Late Archean tonalitic–trondhjemitic–granodiotitic (TTG) batholiths. The Late Archean lithological assemblage, structural style and metamorphic history in the Western Block are similar to those of the Eastern Block. The Trans-North China Orogen is composed of Late Archean to Paleoproterozoic TTG gneisses and granitoids, inter-

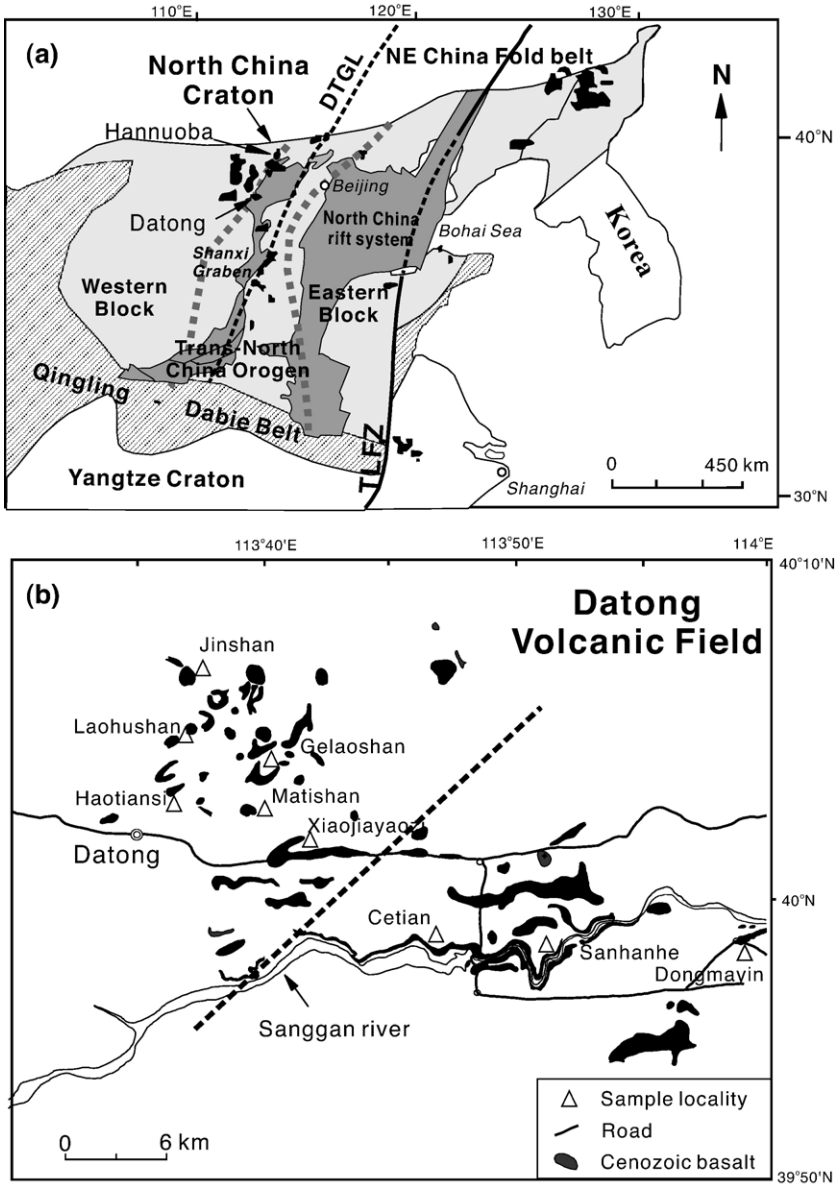

Fig. 1. (a) Simplified tectonic map of the North China Craton; note that the North China Craton is cut by two major geological and geophysical linear zones—Tan-Lu fault zone (TLFZ) to the east and Daxinganlin–Taihangshan gravity lineament (DTGL) to the west. Two shaded and dashed lines outline the Trans-North China Orogen which separates western and eastern Blocks of the North China Craton (after Zhao et al., 2001). The Shaanxi–Shanxi rift system occurs in the Trans-North China Orogen. (b) Distribution of the Quaternary basalts in the Datong volcanic field and sampling localities. The dashed line separates two morphologically and compositionally different parts of the Datong volcanic field.

leaved with abundant sedimentary and volcanic rocks. These rocks underwent compressional deformation and peak high-pressure metamorphism during the Late Paleoproterozoic (2.0–1.8 Ga), as a result of collision between the Western and Eastern Blocks (Zhao et al., 2001).

Recent studies reveal a contrasting geotherm, thickness and composition of the lithospheric mantle beneath the eastern NCC between the Paleozoic and the present time (Griffin et al., 1998; Menzies and Xu, 1998). While diamond inclusions, xenoliths and mineral concentrates in kimberlites indicate a thick (>180 km), cold (<40 mW/m^2) and refractory lithospheric keel beneath the NCC during the Paleozoic, basalt-borne xenoliths reveal a thin (<80 km), hot (~65 mW/m^2) and fertile lithosphere in the Cenozoic. This led to the suggestion of a dramatic change to the lithospheric architecture in the Phanerozoic (Menzies et al., 1993; Griffin et al.,

Table 1
Major element composition (in wt.%) and normative mineral contents in Datong basalts and in international standards

	Tholeiites, east Datong									Alkali basalts, west Datong		
	Cetian			Dongmaying				Sangganhe		Laohushan		
	SDT-5	SDT-6	SDT-7	SDT-8	SDT-10	SDT-12	SDT-13	SDT-31(b)	SDT-32 (t)	SDT-18	SDT-19	SDT-20
SiO_2	51.76	52.28	52.58	52.40	51.90	52.57	51.74	52.07	50.44	49.02	49.37	49.32
TiO_2	2.16	1.94	2.18	1.95	1.81	1.95	1.83	1.88	2.78	2.33	2.35	2.36
Al_2O_3	13.83	13.96	13.73	14.00	14.01	14.20	14.33	14.33	13.96	14.47	14.47	14.49
Fe_2O_3	12.15	12.39	12.23	12.42	12.52	12.37	12.37	12.48	12.92	13.48	13.51	13.69
MgO	6.91	6.55	7.06	6.57	7.37	6.47	7.63	6.57	7.21	6.65	6.79	6.74
MnO	0.15	0.15	0.15	0.15	0.15	0.15	0.15	0.15	0.16	0.17	0.17	0.17
CaO	8.08	8.51	8.05	8.53	8.11	8.48	8.37	8.21	8.22	7.39	7.67	7.52
Na_2O	3.04	2.91	3.39	2.92	2.80	2.90	3.25	3.14	3.04	3.75	3.79	3.89
P_2O_5	0.28	0.21	0.30	0.21	0.19	0.21	0.21	0.21	0.39	0.60	0.60	0.62
K_2O	0.77	0.60	0.76	0.60	0.54	0.58	0.60	0.65	1.03	1.60	1.58	1.64
LOI	−0.47	−0.56	−0.42	−0.36	−0.03	−0.55	−0.49	−0.29	−0.46	−0.86	−0.75	−0.78
Total	98.66	98.94	99.99	99.37	99.33	100.01	99.69	100.15	100.15	98.59	99.55	99.66
Mg#	0.57	0.55	0.58	0.58	0.55	0.59	0.55	0.57	0.57	0.54	0.54	0.54
Na/Ti	3.63	3.87	4.01	3.87	3.99	3.84	4.58	4.31	2.82	4.16	4.15	4.25
Q	4.3	5.3	3.4	5.3	4.5	5.8	1.3	3.7	2.3	0.0	0.0	0.0
Or	4.6	3.5	4.5	3.5	3.2	3.4	3.5	3.8	6.1	9.5	9.3	9.7
Ab	25.7	24.6	28.7	24.7	23.7	24.5	27.5	26.6	25.7	31.7	32.1	32.9
An	21.8	23.3	20.0	23.3	24.1	24.0	22.7	23.1	21.4	17.9	17.8	17.2
Ne	0.0	0.0	0.0	0.0	0.0	0.0	0.0	0.0	0.0	0.0	0.0	0.0
Di	13.3	14.3	14.5	14.3	12.1	13.5	14.1	13.2	13.5	12.0	13.3	13.0
Hy	18.5	18.4	18.3	18.4	22.3	18.5	21.6	19.3	17.9	5.4	4.2	2.2
Ol	0.0	0.0	0.0	0.0	0.0	0.0	0.0	0.0	0.0	10.6	11.3	12.9
Mt	5.3	5.0	5.3	5.0	4.8	5.0	4.8	4.9	6.2	5.6	5.6	5.6
Il	4.1	3.7	4.1	3.7	3.4	3.7	3.5	3.6	5.3	4.4	4.5	4.5
Ap	0.6	0.5	0.7	0.5	0.4	0.5	0.5	0.5	0.9	1.4	1.4	1.4

	Alkali basalts, west Datong									Standards					
	Haotiansi		Jinshan			Xiaojia	Gelaoshan	Matishan		BHVO-2		W-2		MRG-1	
	SDT-14	SDT-17	SDT-22	SDT-23	SDT-24	SDT-34	SDT-35	SDT-36	SDT-37	This work	reference	This work	reference	This work	reference
SiO_2	45.83	50.31	49.09	49.17	47.46	47.66	47.24	47.97	47.97	49.89	49.90	52.38	52.44	39.22	39.12
TiO_2	2.86	2.34	2.40	2.67	2.66	2.89	2.71	3.22	3.07	2.69	2.73	1.10	1.06	3.84	3.77
Al_2O_3	14.38	14.28	14.56	14.33	14.73	15.15	14.43	14.28	14.28	13.26	13.50	15.06	15.35	8.23	8.47
Fe_2O_3	13.85	13.36	13.51	13.63	13.92	13.98	14.03	14.44	13.88	12.21	12.30	10.88	10.74	18.17	17.94
MgO	7.11	6.78	6.74	6.22	6.28	6.15	7.08	6.40	6.39	7.28	7.23	6.46	6.37	13.85	13.55
MnO	0.18	0.17	0.17	0.17	0.17	0.18	0.18	0.18	0.18	0.16	0.17	0.17	0.16	0.16	0.17
CaO	7.87	7.54	7.55	6.87	6.95	6.69	7.91	7.41	7.27	11.49	11.40	10.96	10.87	14.87	14.70
Na_2O	5.11	3.90	3.82	4.23	4.29	3.75	3.13	3.38	3.50	2.20	2.22	2.19	2.14	0.66	0.74
P_2O_5	0.95	0.61	0.64	0.84	0.86	0.87	0.70	0.77	0.71	0.52	0.52	0.61	0.63	0.18	0.18
K_2O	1.21	1.49	1.71	2.21	2.39	2.57	2.00	2.05	2.02	0.27	0.27	0.13	0.13	0.07	0.08
LOI	0.09	−0.80	−0.53	−0.36	−0.36	−0.23	0.30	−0.20	0.07	0.19	0.20	0.57	0.60	1.61	1.56
Total	99.45	99.99	99.67	99.98	99.34	99.89	99.41	100.09	99.25	100.16	100.44	100.50	100.49	100.87	100.28
Mg#	0.55	0.54	0.54	0.52	0.51	0.51	0.54	0.51	0.52						
Na/Ti	4.61	4.29	4.10	4.09	4.16	3.35	2.98	2.71	2.94						
Q	0.0	0.0	0.0	0.0	0.0	0.0	0.0	0.0	0.0						
Or	7.2	8.8	10.1	13.1	14.1	15.2	11.8	12.1	11.9						
Ab	26.7	33.0	32.3	33.4	27.3	29.4	26.5	28.6	29.6						
An	12.7	17.1	17.5	13.6	13.9	16.9	19.4	17.7	17.3						
Ne	9.0	0.0	0.0	1.3	4.9	1.3	0.0	0.0	0.0						
Di	16.2	13.3	12.8	12.2	12.2	8.6	12.3	11.3	11.4						
Hy	0.0	7.8	2.1	0.0	0.0	0.0	3.0	6.7	5.4						
Ol	12.7	8.4	12.7	12.8	13.3	13.7	12.5	7.9	8.6						
Mt	6.3	5.6	5.7	6.0	6.0	6.4	6.1	6.8	6.6						
Il	5.4	4.4	4.6	5.1	5.1	5.5	5.1	6.1	5.8						
Ap	2.2	1.4	1.5	1.9	2.0	2.0	1.6	1.8	1.6						

Mg#=Mg/(Mg+Fe) assuming $Fe_2O_3/(FeO+Fe_2O_3)=0.15$.

b—bottom; t—top; Reference data for BHVO-1, W-2 and MRG-1 are taken from Govindaraju (1989).

1998). This lithospheric destruction may have taken place during the Late Mesozoic (Xu, 2001; Xu et al., 2004b; Wu et al., 2005).

Cenozoic diffuse volcanism is widespread in the Eastern Block and is largely associated with the North China rift system and the Tan-Lu fault (Fig. 1). These basalts and entrained xenoliths are the focus of many studies (Zhou and Armstrong, 1982; Peng et al., 1986; Basu et al., 1991; Fan and Hooper, 1991; Liu et al., 1992, 1994; Tatsumoto et al., 1992; Xu et al., 1996, 2003; Zheng et al., 1998), with recent emphasis on evidence for and mechanism of destruction of the Archean lithospheric keel. In contrast, Cenozoic volcanism is limited in the Western Block and the Trans-North China Orogen. Information about the mantle composition and basaltic petrogenesis in this region is largely based on studies on basalts and included xenoliths from Hannuoba (Song and Frey, 1989; Song et al., 1990; Zhi et al., 1990; Gao et al., 2002; Xu, 2002; Rudnick et al., 2004), which is a southward extension of the Mongolian Plateau volcanism (Barry et al., 2003). As one of the prominent features in the Trans-North China Orogen, the Cenozoic Shaanxi–Shanxi Rift system (Fig. 1) extends from the southern margin of the Loess Plateau north-northeastward across the plateau, delineating a roughly S-shape form. Although rifting started to develop in the southern part of the Shaanxi–Shanxi Rift system in the Late Eocene or Early Oligocene, the major extension occurred in the Neogene and Pleistocene (Ye et al., 1987; Ren et al., 2002). Basaltic volcanism of Oligocene to Pleistocene age occurs in the northern Shaanxi–Shanxi Rift system and adjacent regions.

The Quaternary Datong volcanic field has two morphologically different parts (Fig. 1b). In the west part (north of the Datong county), there are at least 13 volcanic cones (i.e., "the Datong Volcanic Group" named by local geologists), which are mostly composed of volcaniclastic debris with lavas occurring at the base. Preliminary chemical analyses indicated an alkaline affinity for these rocks (Wu and Wang, 1978; Fan et al., 1992). Potassium–Argon (K–Ar) dating suggests that the volcanism in this area began in the Late Pleistocene (0.4 Ma) (Chen et al., 1992). The eastern Datong volcanic field (southeast of the Datong county) includes dominant basaltic lava flows of 3–25 m thick and subordinate volcanic cones along the Sanggan river (Fig. 1b). Volcanic centers commonly occur at intersecting NW- and NE-trending faults. Volcanic cones in this area generally have a lower altitude than those in the west. Basalts are tholeiitic (Wu and Wang, 1978; Fan et al., 1992) and were erupted since the Early Pleistocene (0.74 Ma) (Chen et al., 1992). Samples studied in this paper were collected from Haotiansi, Gelaoshan, Laohushan, Jinshan, Matishan and Xiaojiayaozi (west), Cetian, Sangganhe and Dongmaying (east).

Basalts from west and east Datong volcanic field have different mineralogy. Basalts from eastern Datong volcanic field have olivine (<10%), plagioclase (<10%) and augite (5–10%) as phenocrysts with a groundmass composed of plagioclase (50–70%), basaltic glass (60–90%) and minor olivine (<5%). In contrast, plagioclase and augite phenocrysts are not observed in the samples from west Datong volcanic field, which have a matrix composed of olivine (5–10%) and augite (5–15%) in addition to glass and plagioclase.

3. Analytical methods

The samples were sawed into slabs and the central parts were used for bulk-rock analyses. The rocks were crushed in a steel mortar and ground in a steel mill. Bulk rock abundances of major elements were determined using an X-ray fluorescence spectrometer (XRF) on glass disks at the Guangzhou Institute of Geochemistry, Chinese Academy of Sciences (GIGCAS), following analytical procedures described by Goto and Tatsumi (1996). A pre-ignition was used to determine the loss on ignition (LOI) prior to major element analyses. Analytical uncertainties for majority of major elements analyzed were estimated at smaller than 1% from repeatedly analyzed U.S.G.S. standards BHVO-2, MRG-1 (basalt) and W-2 (diabase). The measured values of international standards are in satisfactory agreement with the recommended values (Table 1). Bulk-rock trace element data [rare earth elements (REE), Sc, Ti, V, Cr, Cs, Sr, Y, Ba, U, Rb, Th, Pb, Zr, Hf, Nb, Ta] were obtained by inductively coupled plasma-mass spectrometry (ICP-MS) at GIGCAS, following the analytical procedures described by Xu (2002). The powders (~50 mg) were dissolved in distilled HF–HNO_3 in Savillex screwtop Telfon breakers at 150 °C for >4 days. Precision for REE and HFSE is estimated to be 5% from repeatedly analyzed U.S.G.S. standards BHVO-1 and W-2 (Xu, 2002).

For Sr–Nd isotopic analyses, sample powders (~100 mg) were dissolved in distilled HF–HNO_3 Savillex screwtop Teflon beakers at 150 °C overnight. Sr and REE were separated on columns made of Sr and REE resins of the Eichrom Company using 0.1% HNO_3 as elutant. Separation of Nd from the REE fractions was carried out on HDEHP columns with a 0.18N HCl elutant. The isotopic analyses were performed using a

Micromass Isoprobe Multi-Collector ICPMS at GIG-CAS. Measured Sr and Nd isotopic ratios were normalized using a $^{86}Sr/^{88}Sr$ value of 0.1194 and a $^{146}Nd/^{144}Nd$ value of 0.7219, respectively. The Sr and Nd blanks during the period of analyses are 0.5 and 0.3 ng, respectively. Analyses of standards during the period of analysis are as follows: NBS987 gave $^{87}Sr/^{86}Sr=0.710243\pm14$ (2σ); Shin Etou gave $^{143}Nd/^{144}Nd=0.512124\pm11$ (2σ), equivalent to a value of 0.511860 for the La Jolla international standard (Tanaka et al., 2004).

4. Results

4.1. Major and minor elements

Major element analyses are in Table 1. According to the nomenclature of Le Bas et al. (1986), the Datong samples are basaltic andesite and trachy-basalt (Fig. 2), but we use the more general classification of tholeiitic and alkali basalts, respectively. CIPW normative calculation further reveals that alkali basalts are olivine-normative, whereas tholeiitic basalts are quartz-normative (Table 1). All samples collected from the western Datong volcanic field have relatively high alkali contents, compared to lavas from the east. This spatial distribution of alkali and tholeiitic basalts was also found by Wu and Wang (1978) and Fan et al. (1992).

The Datong basalts are moderately evolved in having relatively high SiO_2 (45.8–52.6%) and low MgO (6.2–7.4%) contents. In general, tholeiites have higher SiO_2, CaO and MgO and lower Fe_2O_3, TiO_2, Al_2O_3, Na_2O, K_2O and P_2O_5 than alkali basalts (Table 1). There are roughly positive correlations between CaO and MgO (Fig. 3e). No correlation is observed among other oxides (Fig. 3).

For comparison, data for Miocene alkali and tholeiitic basalts from Hannuoba, a type example of Cenozoic basalts in eastern China, are also plotted in Fig. 3. Significant differences in composition are noted between the two lava suites. For example, at a given MgO, Datong alkali and tholeiitic basalts have systematically higher SiO_2, Fe_2O_3 and Cr, lower CaO and Al_2O_3 contents than Hannuoba counterparts, respectively (Fig. 3a, c, d, e, g). High SiO_2 contents of Datong basalts are also reflected by the Q-normative tholeiitic basalts and the lack of Ne-normative alkali basalts (Table 1). In contrast, most tholeiites from Hannuoba are olivine-normative, and alkali basalts are mostly Ne-normative (Ne=2.3% to 11%; Zhi et al., 1990).

4.2. REE and other trace elements

In general, the tholeiitic basalts have lower concentration in incompatible elements than the alkali basalts (Table 2). The alkali and tholeiitic basalts are distinct on chondrite-normalized REE distribution pattern (Fig. 4a, b). The Datong tholeiites are characterized by “kinked” REE patterns with the segment La to Eu and segment Gd to Lu defining different slopes (Fig. 4c). Similar REE patterns have been observed for the tholeiites from Koolau, Hawaii Islands (Frey et al., 1994). Specifically,

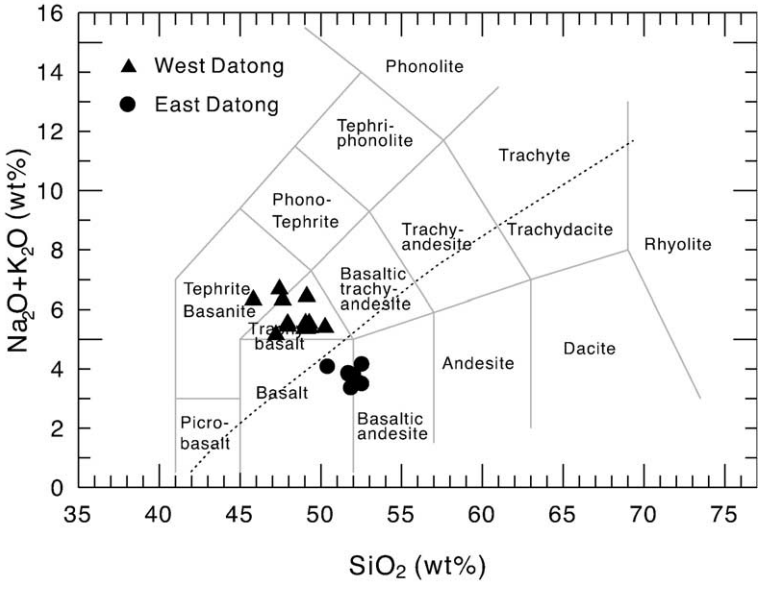

Fig. 2. Na_2O+K_2O versus SiO_2 (Le Bas et al., 1986). Line separating alkali basalts and tholeiites is from McDonald and Katsura (1964).

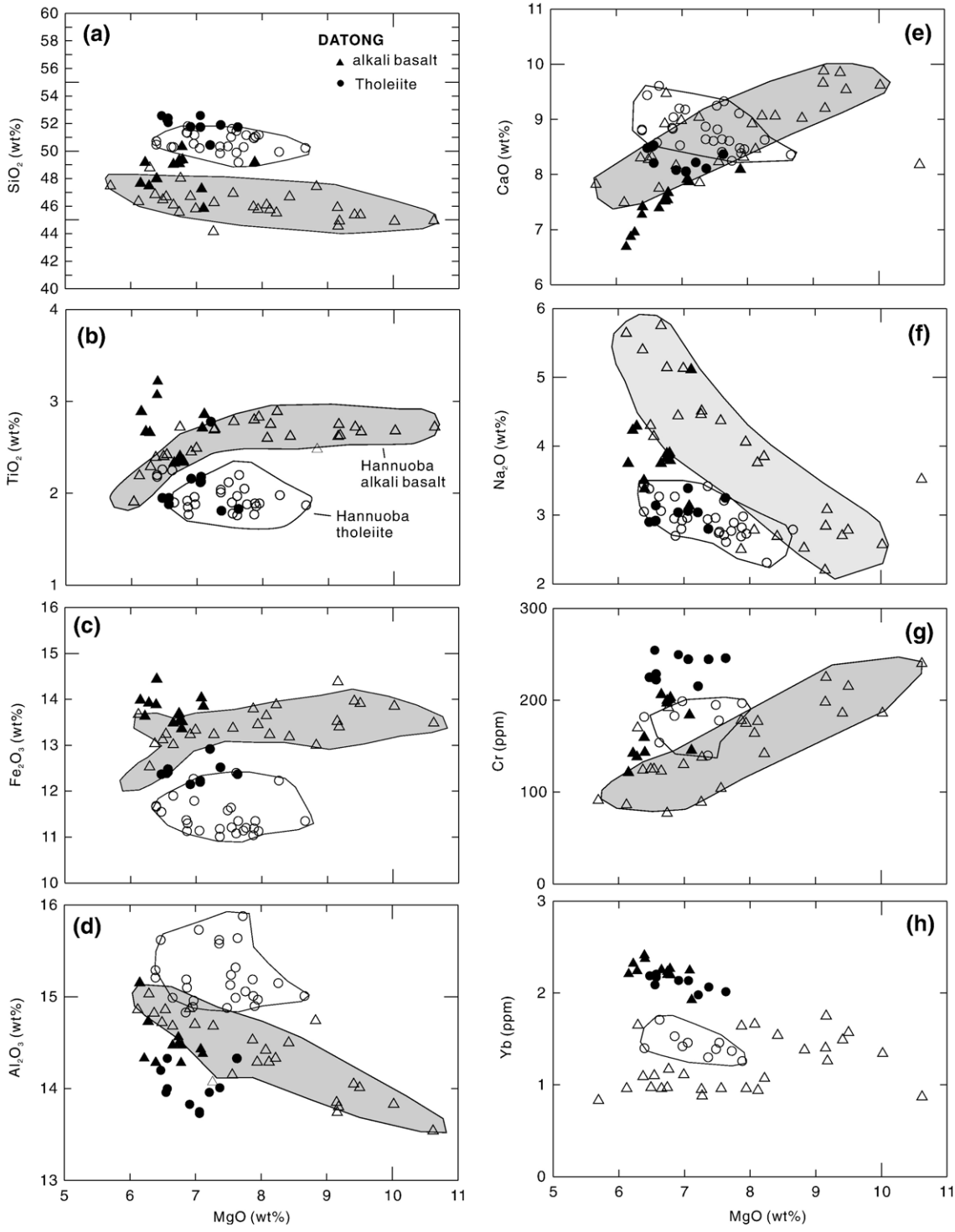

Fig. 3. Variation of SiO_2, TiO_2, TFe_2O_3, Al_2O_3, CaO, Cr and Yb versus MgO for Datong basalts. Also shown are the data for alkali and tholeiitic basalts from Hannuoba (Zhi et al., 1990). Note the higher SiO_2 and lower CaO and Al_2O_3 contents in Datong lavas compared to the Hannuoba samples at given MgO.

Table 2
Trace element composition (in ppm) in Datong basalts

	Tholeiites, east Datong									Alkali basalts, west Datong											
	SDT-5	SDT-6	SDT-7	SDT-8	SDT-10	SDT-12	SDT-13	SDT-31	SDT-32	SDT-14	SDT-17	SDT-18	SDT-19	SDT-20	SDT-22	SDT-23	SDT-24	SDT-34	SDT-35	SDT-36	SDT-37
P	1330	1312	1346	976	902	970	926	989	1803	4219	2740	2686	2757	2820	2912	3924	3853	4072	3181	3627	3287
Sc	20.8	20.7	21.2	22.1	21.0	22.4	21.2	24.3	22.5	15.2	18.7	18.6	18.5	18.6	17.9	16.8	15.9	14.9	18.7	17.6	17.6
Ti	15,294	14,954	15,532	14,009	12,791	13,787	12,686	11,738	17,041	20,553	16,741	16,662	16,665	16,832	17,332	19,215	18,944	18,344	16,462	19,392	18,720
V	167	165	169	174	162	173	164	177.5	190.6	187	158	160	157	158	158	156	153	160	179	172	171
Cr	250	255	245	223	245	225	246	226.4	212.9	145	201	206	203	200	197	142	138	118	181	140	156
Co	42.6	43.6	42.8	42.8	45.6	41.7	44.5	43.68	44.35	44.0	43.3	43.5	43.2	43.2	42.6	41.6	41.8	41.0	43.3	41.9	41.1
Ni	156	157	156	110	137	106	163	159.1	171.7	119	143	144	143	142	138	113	111	108	143	127	130
Ga	21.13	21.10	21.36	20.74	19.99	20.66	20.10	20.49	21.97	26.26	23.65	23.58	23.56	23.78	23.28	25.25	24.99	26.58	22.73	24.57	24.00
Ge	1.67	1.70	1.70	1.65	1.60	1.66	1.60	1.637	1.588	1.53	1.64	1.61	1.66	1.63	1.65	1.62	1.58	1.51	1.49	1.54	1.55
Rb	12.58	12.59	12.16	9.18	8.42	9.33	9.25	9.472	18.54	16.81	24.68	25.33	24.78	27.05	26.91	40.75	40.75	45.55	35.35	39.31	38.98
Sr	373	363	374	285	277	282	286	290.2	513.6	930	629	633	632	632	708	835	875	960	819	764	758
Y	25.82	25.34	26.1	25.66	23.84	25.77	23.31	25.25	24.03	28.96	29.11	28.81	28.63	29.33	29.09	30.75	30.7	31.13	28.03	32.78	32.03
Zr	181	177	183	121	111	120	113	130.1	266.6	348	263	261	259	265	269	331	329	422	352	379	383
Nb	19.75	19.2	19.94	11.1	10.08	11.05	10.45	11.22	35.75	75.26	42.74	42.41	42.52	44.11	45.68	62.4	62.02	76.08	65.31	61.38	59.00
Ba	175	171	175	156	157	154	164	204	285	603	347	367	348	355	378	534	534	625	479	518	503
La	14.24	13.78	14.32	10.44	9.375	10.34	10.12	11.42	18.78	50.94	29.21	29.08	29.24	30.08	31.23	42.84	43.08	48.16	40.43	40.92	37.25
Ce	30.06	29.37	30.17	22.26	20.23	22.16	21.99	24.41	40.10	99.10	59.24	58.45	58.57	60.43	63.14	85.99	84.99	98.72	81.94	85.51	78.84
Pr	4.13	3.94	4.16	3.04	2.79	3.07	2.98	3.35	5.23	12.45	7.52	7.51	7.40	7.70	7.99	10.84	10.71	12.29	10.08	10.77	9.921
Nd	18.89	18.26	18.89	14.49	13.17	14.37	13.71	15.45	23.05	50.36	31.24	31.68	31.26	31.74	32.95	43.84	44.05	52.12	41.58	47.12	43.45
Sm	5.17	5.11	5.26	4.30	3.96	4.25	3.92	4.31	5.81	10.22	7.34	7.36	7.24	7.47	7.63	9.34	9.23	10.69	8.26	9.86	9.36
Eu	1.90	1.84	1.92	1.60	1.51	1.58	1.50	1.59	2.21	3.25	2.51	2.52	2.51	2.56	2.55	3.05	3.00	3.48	2.74	3.33	3.21
Gd	6.43	6.38	6.42	5.85	5.31	5.73	5.33	5.61	6.19	9.49	7.97	7.87	7.84	8.00	7.83	9.08	9.03	9.49	7.75	9.65	9.25
Tb	0.99	0.96	0.99	0.93	0.86	0.91	0.86	0.90	0.96	1.30	1.16	1.16	1.14	1.18	1.17	1.31	1.30	1.44	1.22	1.46	1.37
Dy	5.48	5.39	5.44	5.29	4.78	5.18	4.83	5.16	5.21	6.59	6.17	6.16	6.10	6.21	6.21	6.89	6.76	7.07	6.16	7.35	7.18
Ho	1.02	0.99	1.01	1.00	0.90	0.99	0.90	0.98	0.93	1.12	1.11	1.12	1.09	1.12	1.11	1.22	1.18	1.23	1.11	1.28	1.25
Er	2.47	2.41	2.46	2.49	2.29	2.43	2.28	2.54	2.33	2.57	2.67	2.73	2.65	2.70	2.65	2.87	2.78	2.94	2.73	3.14	3.05
Tm	0.37	0.34	0.35	0.36	0.33	0.36	0.33	0.36	0.32	0.33	0.38	0.38	0.38	0.38	0.37	0.40	0.39	0.38	0.38	0.41	0.40
Yb	2.14	2.09	2.14	2.21	2.07	2.19	2.02	2.16	1.97	1.93	2.26	2.25	2.19	2.23	2.20	2.32	2.24	2.19	2.23	2.36	2.39
Lu	0.31	0.31	0.31	0.33	0.30	0.33	0.30	0.31	0.28	0.26	0.33	0.32	0.32	0.33	0.33	0.33	0.33	0.30	0.31	0.34	0.33
Hf	4.72	4.66	4.77	3.48	3.16	3.41	3.25	3.43	6.14	8.19	6.37	6.34	6.20	6.33	6.46	8.09	7.76	9.34	7.62	8.47	8.45
Ta	1.29	1.27	1.30	0.69	0.64	0.69	0.65	0.71	2.25	4.76	2.66	2.70	2.67	2.73	2.90	4.01	3.94	4.79	4.06	3.84	3.77
Pb	2.08	1.98	1.95	1.66	3.49	1.53	1.68	1.14	1.37	4.21	2.68	2.62	3.83	2.48	2.57	3.66	3.50	2.69	2.87	2.37	2.16
Th	2.03	1.97	2.01	1.11	1.03	1.10	1.06	1.23	3.01	6.59	3.81	3.85	3.82	3.91	4.10	5.54	5.45	6.26	5.58	5.19	5.04
U	0.53	0.53	0.52	0.32	0.28	0.30	0.29	0.32	0.74	1.78	0.95	0.96	0.96	1.03	0.94	1.51	1.48	0.91	1.51	1.34	1.31
Nb/La	1.4	1.4	1.4	1.1	1.1	1.1	1.0	1.0	1.9	1.5	1.5	1.5	1.5	1.5	1.5	1.5	1.4	1.6	1.6	1.5	1.6
Sm/Yb	2.4	2.4	2.5	1.9	1.9	1.9	1.9	2.0	3.0	5.3	3.2	3.3	3.3	3.3	3.5	4.0	4.1	4.9	3.7	4.2	3.9
La/Yb	6.7	6.6	6.7	4.7	4.5	4.7	5.0	5.3	9.5	26.4	12.9	12.9	13.3	13.5	14.2	18.5	19.2	22.0	18.1	17.4	15.6
Ce/Pb	14.4	14.9	15.5	13.5	5.8	14.4	13.1	21.5	29.4	23.6	22.1	22.3	15.3	24.4	24.6	23.5	24.3	36.7	28.5	36.1	36.6
Nb/U	37.4	36.3	38.7	34.9	36.7	37.1	35.7	35.2	48.6	42.3	45.2	44.3	44.2	42.7	48.7	41.4	41.9	83.7	43.2	45.9	44.9

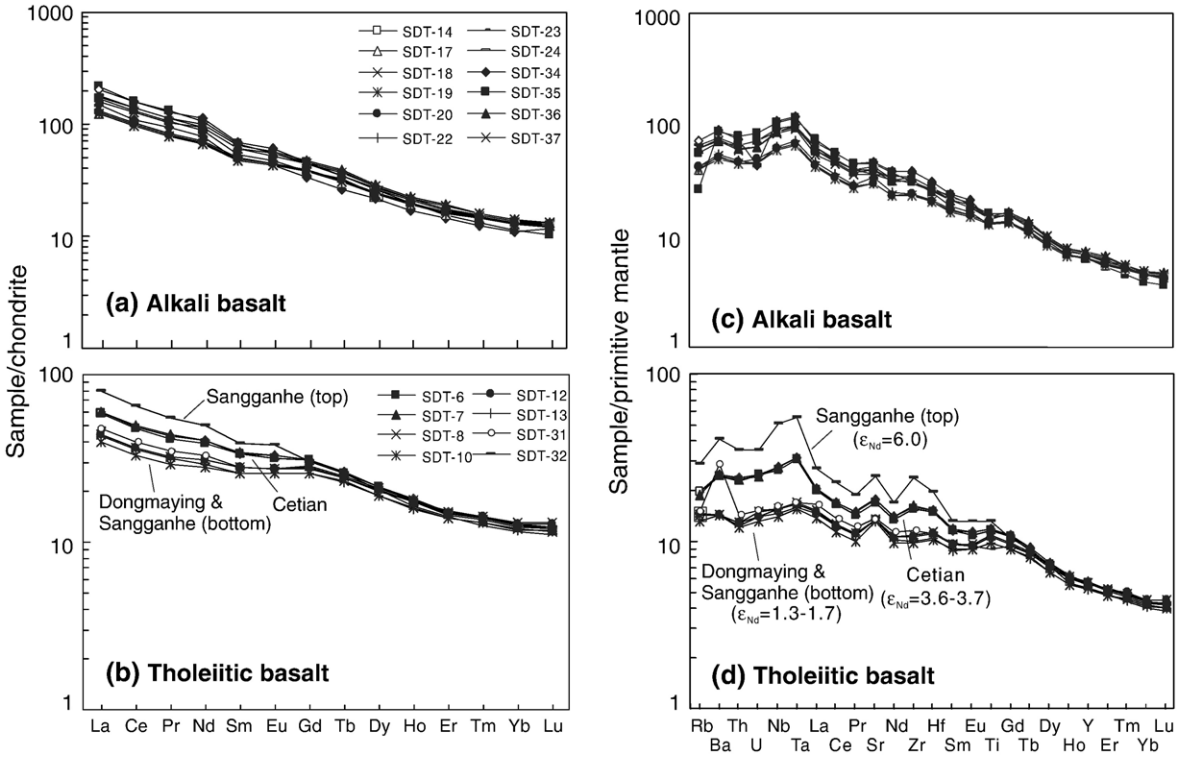

Fig. 4. REE and trace element abundances in whole rocks of the Datong alkali and tholeiitic basalts. The left hand is the REE patterns normalized by chondrite values, the right hand is the spiderdiagrams normalized by primitive mantle values (Sun and McDonough, 1989).

the samples from Cetian (SDT-5, 6, 7) have slightly higher LREE contents [$(La/Yb)_N$=3.1–4.5] than those from Dongmaying (SDT-8, 10, 12, 13) [$(La/Yb)_N$<3]. Two samples from Sangganhe show very different trace element concentrations. While the sample (SDT-31) collected from the bottom of the lava succession has a REE pattern similar to those for Dongmaying basalts, SDT-32 collected at the top of succession shows a distinctly higher concentration in LREE (Fig. 4b). The alkali basalts display a higher LREE-enrichment [$(La/Yb)_N$=8.7–17.9] and a smooth REE pattern without Eu anomaly (Fig. 4a). In the primitive-mantle normalized spidergrams (Fig. 4c, d), tholeiitic basalts show weak, positive Ti, Nb–Ta, Zr–Hf and Sr anomalies. It is interesting to note that the anomalies of these elements increase with the LREE concentration (Fig. 4d). SDT-31 also has an atypical Ba spike. The alkali basalts show a smooth pattern that resembles that of oceanic island basalts (OIB) (Fig. 4c). Both groups show positive Nb–Ta anomalies thereby arguing against the significant crustal involvement in magma genesis.

In general, abundances of Th, U, Rb, Ba, La, Sr and Nd in the Datong lavas are well correlated with Nb (Fig. 5). However, in a small number of samples, there are exceptions. Specifically, SDT-14 and SDT-34 show anomalously low Rb and U, respectively (Fig. 5a, d). The sample from bottom of the Sangganhe section (SDT-31) shows relatively high Ba contents relative to the general correlation (Fig. 5b). Compared to other incompatible elements, Pb shows large scatter (Fig. 5h). SDT-10 and SDT-19 exhibit anomalously high Pb, likely due to the mobility of this element.

4.3. Sr-Nd isotopes

The Sr–Nd isotopic compositions of Datong basalts overlap with OIB (Table 3, Fig. 6a) and define a negative correlation in the Sr–Nd isotopic plot (Fig. 6a). Specifically, the alkali basalts display a rather uniform Sr–Nd isotopic composition (ε_{Nd}=5.4–6.9; $^{87}Sr/^{86}Sr$=0.7034–0.7037), except for SDT-22 which has a relatively high $^{87}Sr/^{86}Sr$ (0.7042). The tholeiitic basalts except SDT-32 display lower ε_{Nd} (1.3–3.7) and higher $^{87}Sr/^{86}Sr$ (0.7039–0.7046). It is surprising to note that there is an inverse correlation between Sm/Nd and ε_{Nd} for Datong basalts. Specifically, Sm/Nd ratio increases from alkali basalt (0.19–0.24), through Cetian tholeiitic basalt (0.27–0.28), to Dongmaying tholeiitic basalt (0.30) (Table 2), but ε_{Nd} increases in

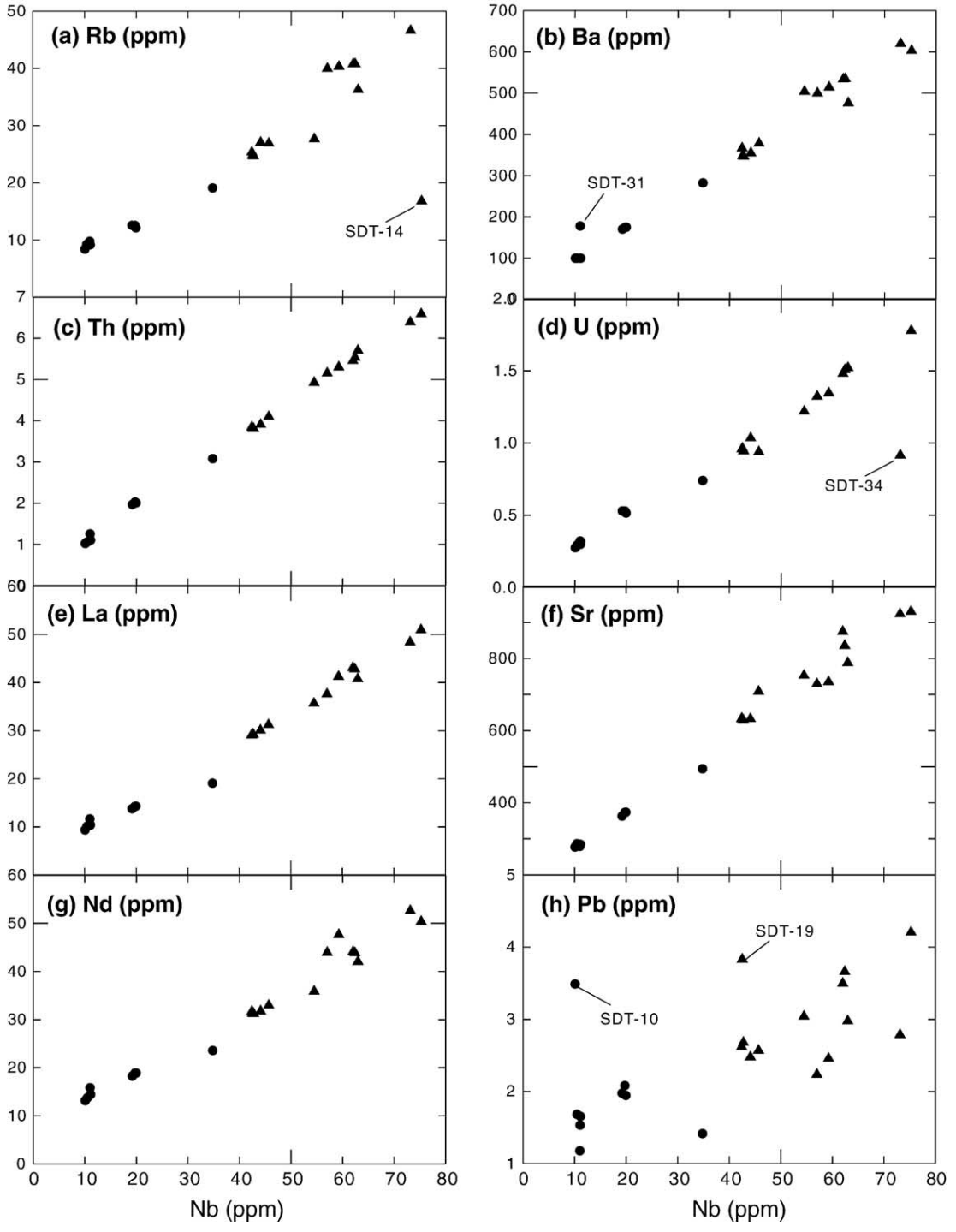

Fig. 5. Variation of selected trace elements versus Nb for the Datong basalts.

the opposite sequence (Table 3). Two tholeiitic samples from Sangganhe also show distinct isotopic composition. While SDT-31 with lower REE concentrations has ε_{Nd} (1.7) similar to those for Dongmaying basalts, SDT-32, which has the highest REE content among the tholeiitic samples, shows isotopic composition ($^{87}Sr/^{86}Sr=0.703563$; $\varepsilon_{Nd}=6.0$) comparable to those observed in alkali basalts. As a whole, the Datong basalts overlap with the isotopic field of the Hannuoba basalts. However, at comparable ε_{Nd}, Datong alkali

Table 3
Sr–Nd isotopic composition of the Datong basalts

	$^{87}Sr/^{86}Sr$	$^{143}Nd/^{144}Nd$	εNd
Tholeiitic basalts, east Datong			
SDT-5	±0.703954 ± 17	0.512826 ± 9	3.7
SDT-6	±0.704007 ± 14	0.512825 ± 9	3.6
SDT-8	±0.704633 ± 15	0.512708 ± 8	1.4
SDT-10	±0.704393 ± 16	0.512723 ± 9	1.7
SDT-12	±0.704502 ± 15	0.512703 ± 10	1.3
SDT-31 (b)	±0.704670 ± 16	0.512725 ± 9	1.7
SDT-32 (t)	±0.703563 ± 15	0.512946 ± 9	6.0
Alkali basalts, west Datong			
SDT-14	±0.703580 ± 14	0.512922 ± 9	5.5
SDT-18	±0.703564 ± 14	0.512917 ± 8	5.4
SDT-19	±0.703650 ± 11	0.512939 ± 13	5.9
SDT-20	±0.703531 ± 13	0.512939 ± 9	5.9
SDT-22	±0.704170 ± 15	0.512958 ± 9	6.2
SDT-24	±0.703749 ± 11	0.512948 ± 8	6.1
SDT-34	±0.703604 ± 14	0.512942 ± 10	5.9
SDT-35	±0.703611 ± 12	0.512914 ± 9	5.4
SDT-36	±0.703368 ± 15	0.512960 ± 8	6.3
SDT-37	±0.703435 ± 11	0.512989 ± 9	6.9

basalts have relatively lower $^{87}Sr/^{86}Sr$ than most Hannuoba samples.

5. Discussion

Compositions of continental basalts are controlled by mantle temperature, lithospheric thickness, source composition and shallow level processes such as crustal contamination, crystal fractionation and post-magmatic modification. The relative importance of these parameters and processes in the generation of Datong basalts will be explored using qualitative and quantitative approaches. Because of their significant geochemical differences, the petrogeneses of the alkali and tholeiitic basalts are addressed separately. Based on petrogenetic interpretation, a model is developed to account for the spatial distribution of the two lava suites.

5.1. Effect of post-magmatic alteration on magma compositions

The Datong lavas are Quaternary in age and are generally very fresh. This is reflected by the absence of alteration feature in thin section, negative loss on ignition (LOI) values (Table 1), and the good correlation between abundances of Th, U, Rb, Ba, Sr, Pb, Nd, La and Nb (Fig. 5). It is concluded that most highly incompatible elements such as Rb, which are commonly mobile during surface processes, were not affected by post-magmatic processes. The effect of post-magmatic processes, if any, is limited to some alkali metals and Pb in a small number of samples; for example, the deviation of sample SDT-14 in the Rb–Nb plot (Fig. 5a) and SDT-31 in Ba–Nb plot (Fig. 5b), and the deviation of SDT-34 in the U–Nb plot. Also two samples (SDT-10, SDT-19) are characterized by anomalously high Pb contents relative to the bulk correlation (Fig. 5h). Although low Ce/Pb may result from crustal contamination, sample SDT-19 has Sr–Nd isotopic ratios similar to other alkali basalts, which have Ce/Pb ratios well within the average values of oceanic basalts (Fig. 7a). Consequently, anomalously high Pb content in SDT-19 may reflect mobility of Pb during surface processes. A similar conclusion can be made for Pb in SDT-10.

5.2. Alkali basalts: magmas derived from the convective asthenosphere

5.2.1. Evidence for an asthenospheric source

A convective asthenospheric origin has been inferred by previous geochemical studies on Cenozoic alkali basalts from eastern China (Zhi et al., 1990; Song et al., 1990; Basu et al., 1991; Liu et al., 1994; Zou et al., 2000). A similar petrogenetic interpretation also applies in the case of the Datong alkali basalts given the following observations. The presence of peridotite xenoliths in the Datong alkali basalts (Chen et al., 1997) suggests rapid ascent of magma to the surface, thereby avoiding a long residence time at crustal levels. Limited interaction with the lithosphere is also reflected by their homogeneous Sr–Nd isotopic composition that is well within the field of OIB (Fig. 6a). The average Ce/Pb and Nb/U ratios of oceanic basalts (OIB and MORB) are 25 ± 5 and 47 ± 7, respectively (Hofmann et al., 1986), significantly higher than the value for average continental crust or arc volcanic rocks (Taylor and McLennan, 1985). These elements are not fractionated from each other during partial melting or fractional crystallization and their ratios reflect those of source regions (Hofmann, 1988). Despite their relatively evolved characteristics, Datong alkali basalts have virtually constant Ce/Pb (except for the samples whose Pb may have been affected by post-magmatic processes) and Nb/U ratios (Fig. 7a, b). Moreover, these ratios are close to the average values of OIB and MORB, strongly suggesting that Datong alkali basalts share a similar source with oceanic basalts.

Ba/Nb and La/Nb ratios in Datong alkali basalts range from 7.3 to 8.6 and 0.62 to 0.69, respectively (Table 2), overlapping the OIB field and are significantly different from that of MORB (Fig. 7c). This is indicative of an enriched source for Datong basalts.

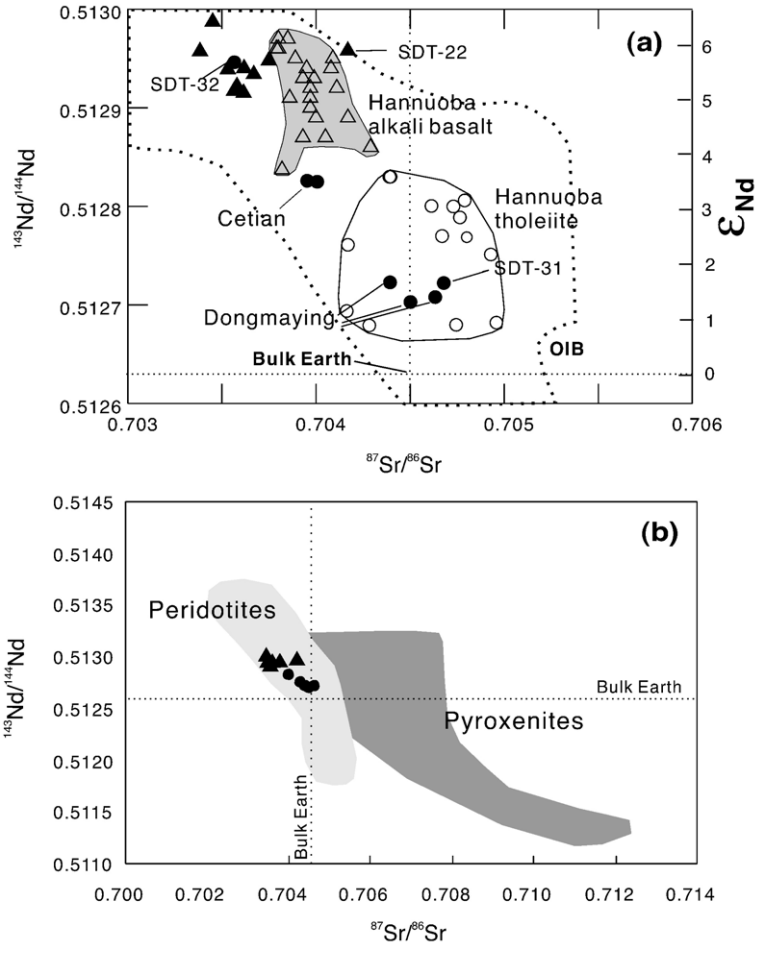

Fig. 6. (a) $^{87}Sr/^{86}Sr$ versus ε_{Nd} of the Datong basalts. Isotope data of the basalts from Hannuoba (Song et al., 1990) are given for comparison. Isotopic range of oceanic island basalts (OIB) is after Zindler and Hart (1986). (b) Comparison of isotopic composition of the Datong basalts with those of mantle xenoliths in Cenozoic basalts from North China. Data source: Song and Frey (1989), Tatsumoto et al. (1992), Xu et al. (1998, 2003), Fan et al. (2000) and Xu (2002).

Given the time-integrated, depleted Sr–Nd isotopic ratios of these lavas, it is apparent that the enrichment process was recent. The enrichment process likely took place through infiltration of incompatible element and volatile-rich metasomatic melts or fluids from the deeper asthenosphere.

5.2.2. Source characteristics constrained by REE modeling

A plot of La/Yb against Sm/Yb can be used to distinguish between melting of spinel and garnet peridotite. Because Yb is compatible in garnet, whereas La and Sm are incompatible, La/Yb and Sm/Yb will be strongly fractionated when melting degree is low. In contrast, La/Yb is only slightly fractionated and Sm/Yb is nearly unfractionated during the melting in the spinel stability field. Fig. 8a shows that variable degrees (5–20%) of batch melting of a hypothetical light REE-enriched mantle source ($[La/Yb]_n > 1$) in the garnet stability field can generate the La/Yb–Sm/Yb systematics of Datong alkali and tholeiitic basalts. Specifically, alkali basalts have lower degree of melting (5–10%) than tholeiitic basalts (14–22%).

Inverse modeling of REE also leads to the conclusion that garnet is required in source of Datong basalts (Fig. 8b, c). Following the method described in the Appendix, the lava compositions were corrected to primary magma compositions by using least squares modeling of major elements. Fractionation-corrected REE concentrations were plotted in "process identification" diagrams and the slopes and intercept and various melting reactions were input to calculate source REE concentrations and bulk solid/melt partition

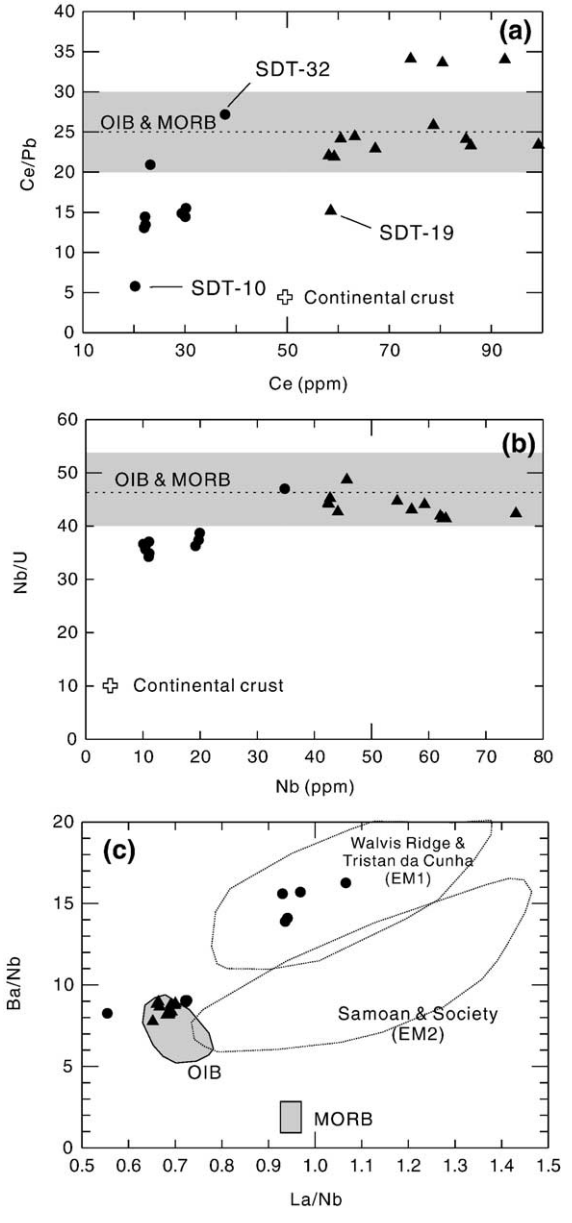

Fig. 7. (a) Ce/Pb versus Ce; (b) Nb/U versus Nb; (c) Ba/Nb versus La/Nb. The average ratios of Nb/U and Ce/Pb in OIB and MORB are after Hofmann et al. (1986). Fields of OIB and EM in (c) are from Weaver (1991) and Liu et al. (1994).

coefficients relative to the La concentration in the initial source (Fig. 8b). The steadily increasing values for D_o^i from La to Lu (Fig. 8b) reflect an important contribution from garnet in the source. Comparison of Fig. 8a, b indicates that there are convergent solutions derived from inverse and forward modeling, that is, an enriched source with residual garnet and clinopyroxene can reproduce the relative REE abundance of Datong alkali basalts by batch melting.

5.2.3. Compositional difference between Datong and Hannuoba basalts

The Datong basalts differ in major element composition from Hannuoba basalts (Fig. 3). Specifically, at a given MgO, Datong lavas have higher SiO_2 and lower Al_2O_3 and CaO. These compositional differences may reflect differences in source composition, melting conditions and post-melting fractionation processes.

Datong alkali basalts are low in MgO (mostly <6.8%), Mg# (0.52–0.55) and Ni contents (<143 ppm). They are far from the expected composition of melts in equilibrium with mantle peridotites (Frey et al., 1978; Cox, 1980), and they may have undergone extensive crystal fractionation. The mantle-derived peridotite xenoliths in these lavas (Chen et al., 1997) suggest that crystal fractionation occurred within the upper mantle before incorporation of the xenoliths. High-pressure fractionation is consistent with the lack of plagioclase fractionation in Datong lavas as evidenced by the positive correlation of Sr with Nb (Fig. 5f) and lack of Sr and Eu anomalies in spider diagram (Fig. 4c). The positive correlation of CaO with MgO (Fig. 3e) and relatively low Ni content suggest a fractionating assemblage of clinopyroxene and olivine, which is different from the eclogitic fractionation associated with Hannuoba basalts (Zhi et al., 1990). However, different fractionation processes are not responsible for the compositional contrast between the two lava suites. For example, fractionation of garnet in Hannuoba lavas is expected to produce a melt with lower Al_2O_3 content than Datong basalts. In fact, an opposite trend is noted in Fig. 3d.

The compositional differences between Datong and Hannuoba lavas are likely related to different melting conditions in the two localities. It is widely accepted that the melting pressure has an effect on the degree of silica saturation of the magmas (Takahashi and Kushiro, 1983; Langmuir et al., 1992; Kushiro, 2001). Specifically, small degrees of partial melting at high pressure produces magmas with more normative nepheline (Ne), while large degree of melting at lower pressure produce magmas with normative hypersthene and quartz (DePaolo and Daley, 2000). In contrast with the relatively high Ne-normative contents (2.3% to 11%) in Hannuoba alkali basalts (Zhi et al., 1990), most of Datong alkali basalts have no Ne content (Table 1). As shown in Fig. 8a, the Datong basalts were formed by higher degrees of melting than the Hannuoba basalts for a given basalt type. Since melting degree is inversely proportional to melting depth (Langmuir et al., 1992), it is inferred that the Datong basalts may have

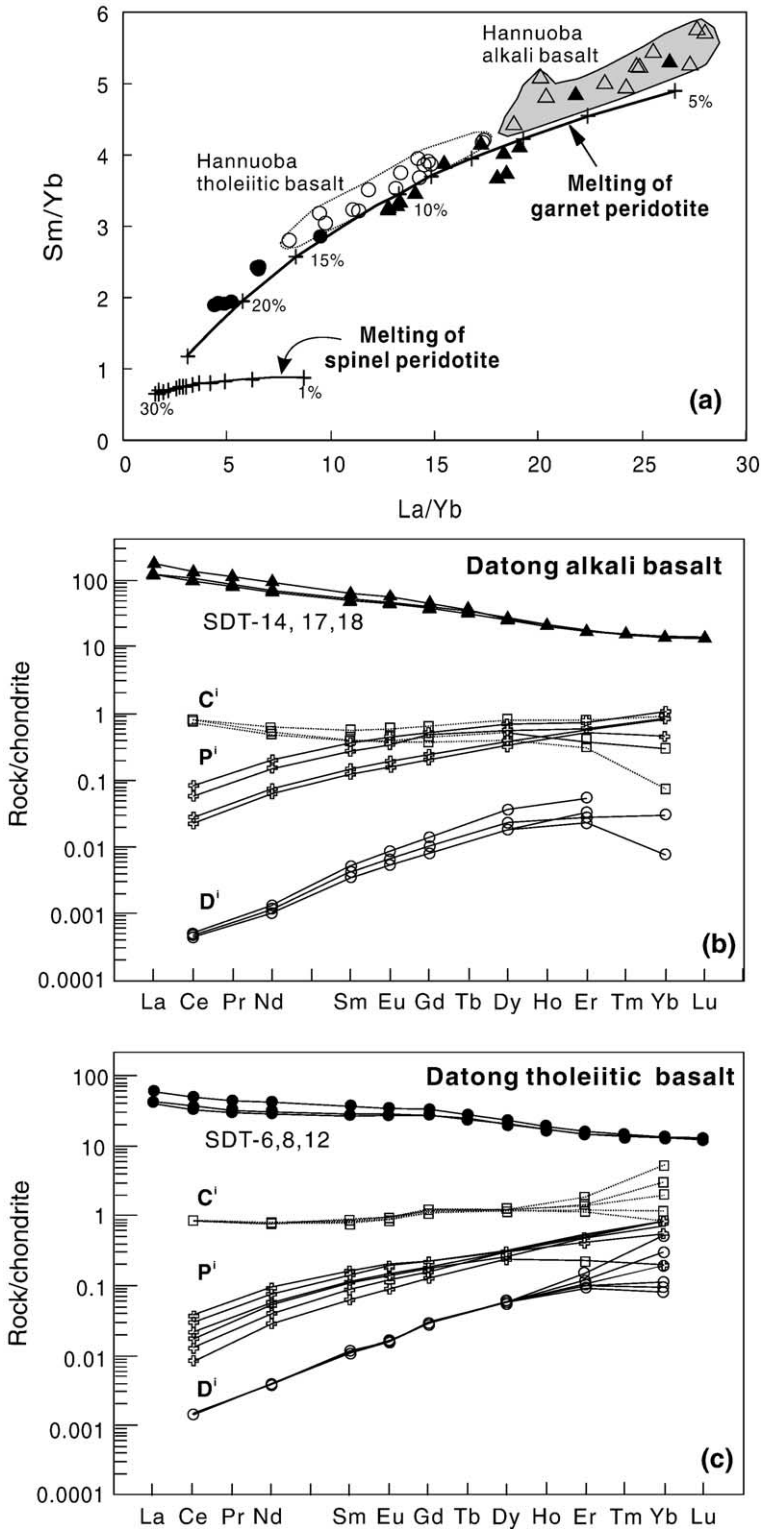

Fig. 8. (a) La/Yb vs Sm/Yb for the Datong basalts. Also shown are batch melting curves calculated for garnet peridotite and spinel peridotite. Partition coefficients are taken from Johnson et al. (1990). The starting materials are ol, 55%; opx, 20%; cpx, 15%; gt, 10%; melting reaction in garnet field (Walter, 1998): ol, 3%; opx, 3%; cpx, 70%; gt, 24%; melting reaction in spinel field (Kinzler, 1997): ol, −6%; opx, 28%; cpx, 67%; sp, 11%. (b) Inversion results for Datong alkali basalts. (c) Inversion results for Datong tholeiitic basalts. Initial concentration and partition coefficients relative to La were calculated for fractionation-corrected Datong alkali basalts using inverse technique described by Feigenson et al. (2003).

been formed at shallower depth than the Hannuoba basalts.

Differences in melting depth are also evident in Na/Ti, a ratio that is sensitive to the pressure of melt segregation (Putirka, 1999a). Na/Ti of melts decreases with increasing mean pressure, because $D_{Na}^{cpx/melt}$ increases with increasing pressure (Blundy et al., 1995; Kinzler, 1997), while clinopyroxene and garnet $D_{Ti}^{mineral/melt}$ remain constant or decrease (Kinzler, 1997; Putirka, 1999a). Na/Ti ratios for Hannuoba alkali basalts increase with decreasing MgO for the samples with MgO<8% (Fig. 9a), suggesting that they have been affected by crystal fractionation. Increasing Na/Ti during the differentiation was related to a decrease in Ti content as a result of fractionation of Ti-oxides, clinopyroxene and garnet (Fig. 3b; Zhi et al., 1990). It is noted that the Hannuoba samples with MgO>8% have rather constant Na/Ti ratios (~2.5; Fig. 9a) and we assume that these are those of primitive magma. In contrast, Datong alkali basalts have relatively high

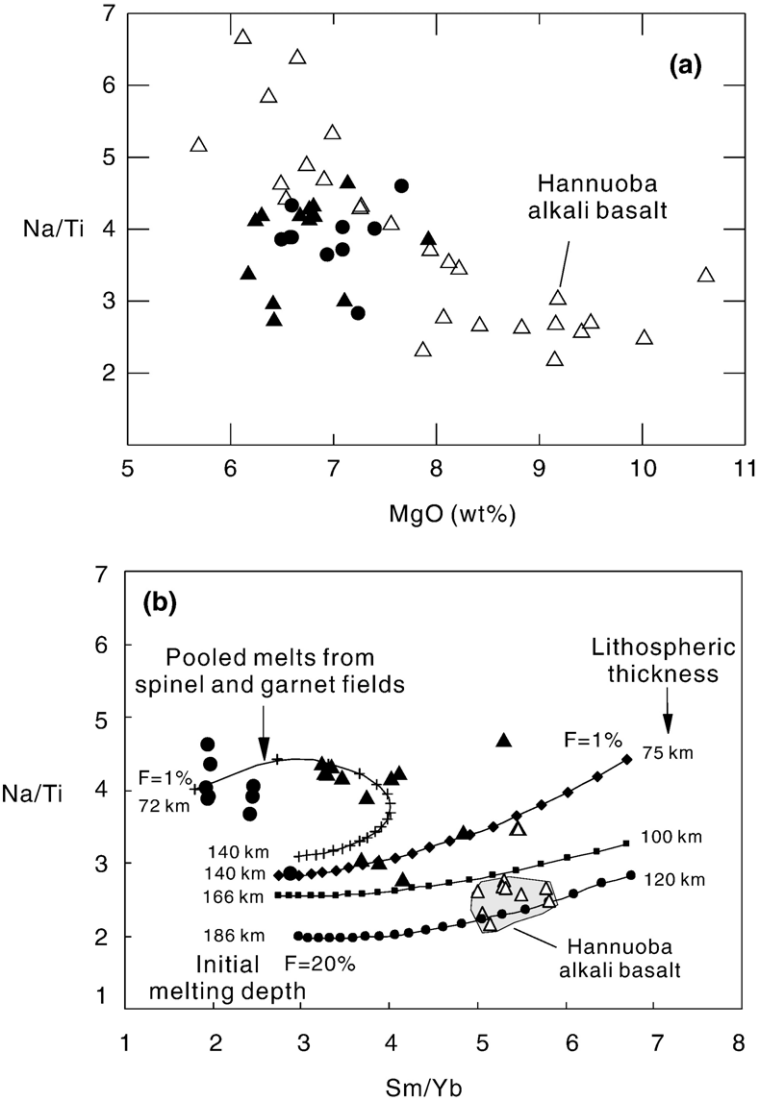

Fig. 9. (a) Variation of Na/Ti cation fraction ratios with MgO for the alkali basalts from Datong and Hannuoba. For Datong samples, Na/Ti ratios are insensitive to MgO content. In contrast, roughly negative correlation indicates the effect of low-pressure fractionation on Na/Ti ratio in the Hannuoba basalts. Only samples with >8 wt.% MgO show relatively constant ratios and are considered in (b). (b) The composition of aggregate magmas generated from variable lithospheric thickness and initial melting depth in comparison with the Datong and Hannuoba basalts. Melting trajectories are calculated following the approach described by Kinzler (1997) and Putirka (1999a). The markers in each trajectory represent increment of 1% melting. The partition coefficients are from Johnson (1998) and Putirka (1999b). Source mineralogy and melting reactions are the same as in the caption of Fig. 8. Decompression reaction of garnet is after Johnson et al. (1990): 0.17 ol+gt=0.53 opx+0.47 cpx+0.17 sp.

Na/Ti ratio (ranging from 2.7–4.6 with an average of 3.82), irrespective of MgO contents. Such a high Na/Ti ratio cannot be related to the fractionation of high-pressure clinopyroxene inferred for Datong basalts, because such fractionation would lead to decrease in Na/Ti in residual melts (Putirka, 1999a). Therefore, as also indicated by differences in normative Ne, the differences in Na/Ti suggest that the pressure of melt segregation for Datong alkali basalts is less than that of Hannuoba alkali basalts.

Surprisingly, other pressure-sensitive elements such as Fe do not show a significant difference between Datong and Hannuoba basalts. Perhaps, the lower Fe content expected for the lower pressure Datong basalts was increased by clinopyroxene and olivine fractionation. Different melting pressures however cannot account for the lower CaO and Al_2O_3 contents in Datong lavas compared to Hannuoba basalts. If Hannuoba alkali basalts were segregated at a higher mean pressure, they should have lower Al_2O_3 contents, because Al_2O_3 is partially retained in residual garnet. Lower CaO contents are also expected in Hannuoba basalts because CaO content of melts in equilibrium with garnet peridotites increases with increasing pressure (Frey et al., 1994). In fact, opposite trends are observed for Datong and Hannuoba basalts. In this regard, the two lava suites may have been derived from different sources; Datong basalts were derived from a more refractory source that was already depleted in CaO and Al_2O_3. This inference is consistent with slightly lower $^{87}Sr/^{86}Sr$ ratios of Datong alkali basalts compared to Hannuoba samples (Fig. 6a).

However, a more depleted source for Datong alkali basalt is not consistent with their high Na/Ti (Fig. 9a) and Yb content (Fig. 3h). Therefore, we infer that Na/Ti and Yb reflect lower pressure of melt segregation for Datong alkali basalt, whereas CaO and Al_2O_3 reflect the more depleted nature of the source of Datong alkali basalts.

5.2.4. Evidence for Cenozoic lithospheric thinning in western NCC

A comparison of the Na/Ti and Sm/Yb ratios with the calculated melting trajectories (Fig. 9b) provides quantitative constraints on melting depth and lithospheric thickness. The calculation was performed following Kinzler (1997) and Putirka (1999a) for melting that starts at the depth where the adiabatic geotherm crosses the mantle solidus and ends at the lithosphere–asthenosphere boundary. Melting rate is assumed to be 0.01/kbar (Langmuir et al., 1992) and melts segregate from residues at $F=0.01$. In this sense, melting is "near-fractional" and can be approximated as incremental batch melting, with 1% increments of melt being produced and segregated with each 1 kbar rise of the mantle above the starting depth. Since the calculated composition of aggregate magmas is sensitive to source composition, only the relative range imposed by different lithospheric thickness and initial melting depth is emphasized. The depth of the spinel to garnet transition at the peridotite solidus is assumed at ~75 km following McKenzie and O'Nions (1991)'s rational, although recent experimental studies suggest a greater depth (80–85 km, Robinson and Wood, 1998; Klemme and O'Neill, 2000).

As discussed earlier, the source for Datong alkali basalt differs from that for Hannuoba basalts, so different Sm/Yb and Na/Ti ratios were used for the sources of two lava suites. The calculated Sm/Yb trajectory in Fig. 9b was obtained by varying Sm/Yb of the source to meet the requirement that the melting degree of alkali basalts is less than 10%. Hannuoba basalts are within melting trajectories for assumed lithospheric thickness of 100 to 120 km (Fig. 9b). We prefer this range of lithospheric thickness because with a thicker lithosphere, higher mean pressure of melt segregation will generate strongly Si-understaured melts (Kushiro, 2001) unlike Hannuoba alkali basalts, and require >10% melting for Datong alkali basalts. On the other hand, a thinner lithosphere for Hannuoba alkali basalts places Datong alkali basalts completely within the spinel stability field, a result inconsistent with the REE modeling results (Fig. 8). We conclude that a lithospheric thickness of about 100 km is a reasonable estimate for Hannuoba basalts. If the spinel–garnet transition occurs at ~75 km (McKenzie and O'Nions, 1991), the Datong data are within the field of spinel peridotites at a thickness of 72 km. However, if melting began within the garnet stability field and continued into the spinel field, modeling with a lithospheric thickness of 72 km (Fig. 9b) shows that at a high degree of melting, the composition of aggregated magmas is dominated by melts derived from garnet peridotite, whereas at a low degree of melting, melt composition is significantly influenced by melts derived in the spinel field. In this case, the partial melting degree is estimated to be 3–5% for Datong alkali basalts (Fig. 9b). In conclusion, at the time of eruption of the Datong basalts, the lithosphere was confined to the spinel field, but its base was not far from the spinel–garnet transition zone. This conclusion is broadly consistent with the presence of tholeiite at Datong, which has an asthenospheric signature (i.e., SDT-32). According to DePaolo and Daley (2000), the lithosphere is >80 km

thick if the alkali basalts have a continental lithospheric mantle isotopic signature; the lithosphere is inferred to be <60 km thick if the tholeiitic basalts have an asthenospheric signature.

The estimate of about 70 km for lithospheric thickness during Datong volcanism is significantly thinner than that (~100 km) associated with the Hannuoba basalts. Since the Hannuoba basalts were erupted during the Miocene and the Datong lavas were emplaced in the Quaternary, this mirrors the progressive lithospheric thinning in western NCC during the Cenozoic (Xu et al., 2004a). This contrasts with the Cenozoic lithospheric accretion in eastern NCC (Xu, 2001), probably due to diachronous extension in the NCC, with extension first in the eastern NCC owing to the Late Mesozoic Paleo-Pacific subduction and then migrating to the western NNC induced by the Early Tertiary Indian–Eurasian collision (Xu et al., 2004a).

5.3. Tholeiitic basalts: products of lithosphere–asthenosphere interaction

5.3.1. Crustal contamination?

Like the Hannuoba basalts, tholeiitic basalts from Datong have higher $^{87}Sr/^{86}Sr$ and lower ε_{Nd} than the associated alkali basalts. This precludes a simple genetic relationship between alkali and tholeiitic basalts via fractional crystallization. The inverse ε_{Nd}–Sm/Nd trend (Fig. 10a) and positive $^{87}Sr/^{86}Sr$–1/Sr correlation (Fig. 10b) are consistent with mixing of two isotopically distinct components. Given the compositional similarity between the tholeiitic sample (SDT-32) and bulk of alkali basalts (Fig. 10b), it is possible that the component with low $^{87}Sr/^{86}Sr$ and high ε_{Nd} is plausibly from the asthenosphere. Another mixing component, characterized by high $^{87}Sr/^{86}Sr$ and low ε_{Nd} and Ce/Pb may either be from the crust or the lithospheric mantle, or both.

Country rocks in North China are Archean metamorphic rocks, Jurassic sediments and granites and Cretaceous to Quaternary sediments (Zhi et al., 1990). Therefore, melts/fluids derived from the upper and lower crust are possible contaminants. If the upper crust was involved in the genesis of tholeiites, the most contaminated samples with the lowest ε_{Nd} would also display the lowest Sm/Nd (Fig. 10b), because upper crust is generally characterized by LILE-enrichment (low Sm/Nd) and HFSE-depletion. The negative correlation between ε_{Nd} and Sm/Nd for Datong tholeiitic basalts is opposite to this expected trend (Fig. 10b). Mass balance calculation shows that, to reduce the concentration of Nb in an OIB magma from 50 to 10–20 ppm range characteristic of the Datong tholeiites requires addition of >150% crustal material. Such large quantities of crust would not yield a basaltic composition. Moreover, Datong tholeiitic basalt does not have the low Nb/La that is characteristic of continental crust. Other geochemical data are inconsistent with shallow magma chamber process in which crystal fractionation and assimilation of upper crustal rocks are coupled (DePaolo, 1981). For example, there is no correlation between MgO and ε_{Nd} (Fig. 10c) and all Datong tholeiitic basalts have >220 ppm Cr (Fig. 3g).

Song et al. (1990) noted that granulites from North China and worldwide localities do not lie along the mixing trends defined by the Hannuoba basalts. They argued against a role of contamination by lower crust. A similar argument can be made for Datong tholeiites because they exhibit a Sr–Nd isotopic correlation that is similar to that for the Hannuoba basalts (Fig. 6).

5.3.2. Formation of tholeiitic basalts by melt–lithospheric mantle reaction

It is widely accepted that the compositions of quartz tholeiites reflect segregation from peridotite at 10–15 kbar (Kushiro, 2001), corresponding to a depth of about 35–50 km. Even when the effects of minor constituents, such as K_2O and H_2O, are considered, the maximum melt segregation depth of Q-normative tholeiites is about 60 km (DePaolo and Daley, 2000). This depth is significantly shallower than the low velocity zone in the NCC (70–105 km, Ma, 1989; Chen et al., 1991) and the lithospheric thickness inferred from alkali basalt geochemistry (Fig. 9b). Consequently, generation of Datong tholeiitic basalts likely occurred within the lithospheric mantle or at the lithosphere–asthenosphere boundary.

On the other hand, a shallow melting depth (<60 km) for quartz tholeiites places the source of Datong tholeiites within the stability field of spinel peridotite, given the spinel–garnet transition at ~75 km (O'Neill, 1981). However, a garnet-bearing source is required by modeling of REE systematics (Fig. 8a, c). The explanation invoked for alkali basalts, i.e., melting began within the garnet stability field and continued into the spinel field, is not applicable for tholeiites. This is because at a large degree of melting and at a final melting depth at ~60 km, the composition of aggregated magmas is dominated by melts derived from spinel peridotite. Alternatively, the garnet signature may arise from garnet pyroxenite veins and layers in peridotitic mantle (e.g., Hauri, 1996; Hirschmann and Stopler, 1996). Although pyroxenites are extremely

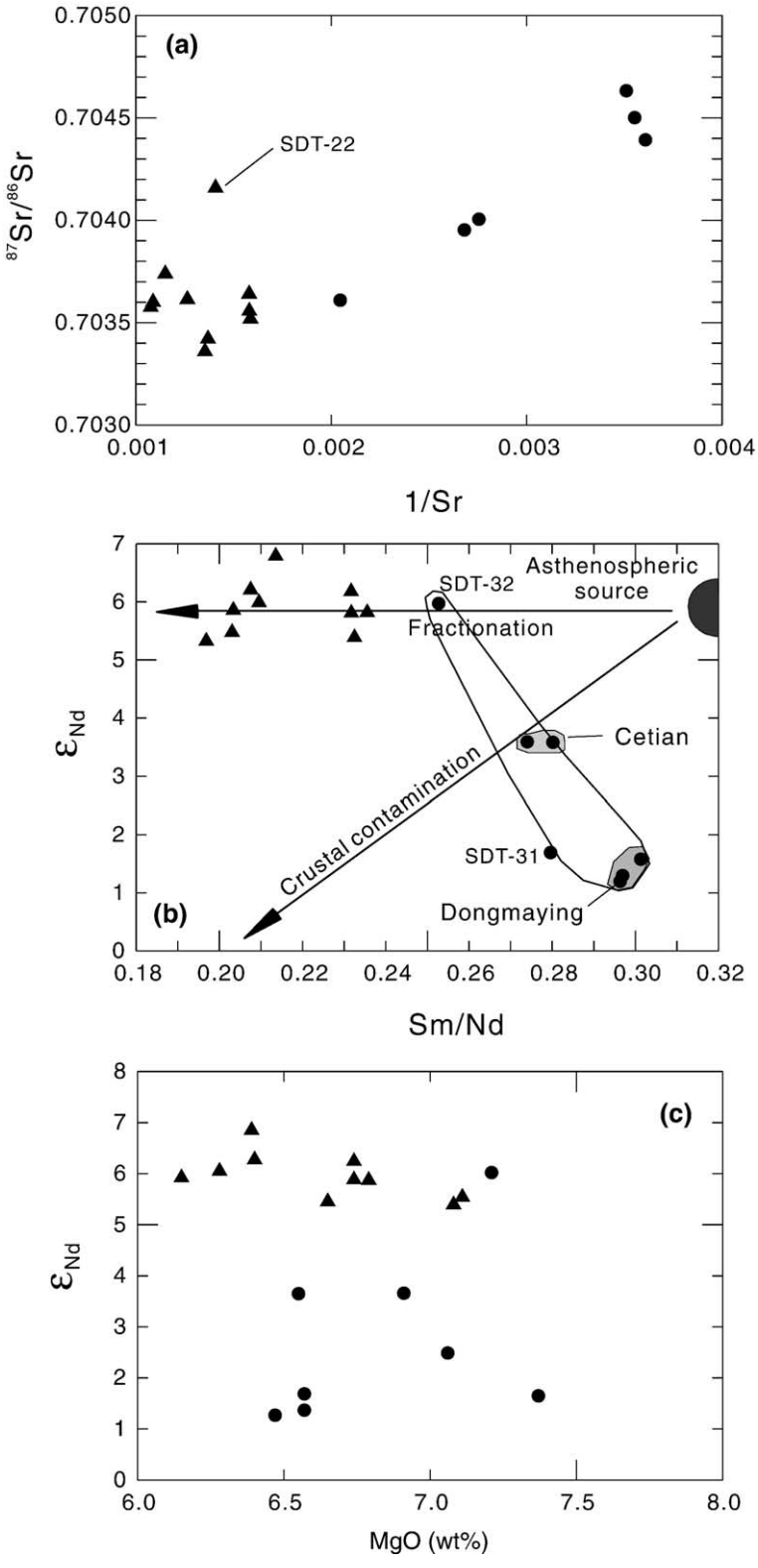

Fig. 10. Plots showing a two-component mixing trend for the Datong basalts. (a) $^{87}Sr/^{86}Sr$ versus $1/Sr$; (b) ε_{Nd} versus Sm/Nd; (c) ε_{Nd} versus MgO.

heterogeneous in isotopic composition, they generally show EM2-type signature (Tatsumoto et al., 1992; Xu, 2002; Fig. 6b), whereas an EM1 component was involved in Cenozoic basalts from North China (Basu et al., 1991; Liu et al., 1994; Zou et al., 2000).

This contradiction, major element composition indicating melt segregation within spinel peridotite field but REE geochemistry requiring control by residual garnet, is reminiscent of the paradox encountered in Hawaiian tholeiites (Eggins, 1992a). Eggins (1992b) showed that the Hawaiian tholeiites cannot be produced solely by melting of an upwelling plume. Wagner and Grove (1998) reached a similar conclusion on the experimental grounds and further proposed a two-stage model, in which primary tholeiites, generated by partial melting of garnet lherzolite in a mantle plume, reacted with harzburgite in the mantle by assimilating orthopyroxene and crystallizing olivine. A similar model is adopted here, because during thermomechanical thinning/erosion of the mantle lithosphere by upwelling plume/asthenosphere, basaltic melts will infiltrate into lithosphere and react with peridotites. This is the likely scenario under which Datong tholeiitic basalts were formed. Moreover, interaction of alkali basalt with refractory peridotites can explain the main geochemical characteristics of Datong tholeiitic basalts.

(1) As outlined previously, Datong tholeiitic basalts with a moderate MgO content (~6–7%) have Cr contents similar to high MgO (~11%) lavas from Hannuoba (Fig. 3g). Enrichment of Cr in moderately evolved basaltic lavas is enigmatic given its compatible nature in clinopyroxene. However, anomalously high Cr can result from melt/peridotite reaction (Kelemen et al., 1992; Godard et al., 1995). Godard et al. (1995) demonstrated that the trace element contents of peridotites affected by melt–rock reaction involving mineralogical change are controlled both by peridotite/melt and intermineral partition coefficients. Consequently, elements with distinct peridotite/melt partition coefficients but similar intermineral partitioning (e.g., Cr and REE, both dominantly hosted in pyroxenes) behave in a similar fashion during melt–rock reaction involving pyroxene dissolution and olivine crystallization. The incompatible behavior of Cr has been documented in various suites of "reactive" mantle rocks from ophiolites (Rampone et al., 2004), orogenic peridotite massifs (Van der Wal and Bodinier, 1996) and xenoliths (Xu et al., 2003). Consequently, the Cr content of residual melts after reaction with peridotite is expected to increase due to pyroxene dissolution. In addition to explaining relatively high Cr contents, an olivine-forming, pyroxene-dissolving reaction will also increase the SiO_2 contents of melts.

(2) Another striking compositional feature displayed by the Datong lavas is their "kinked" REE pattern (Fig. 4b). At a first sight, this REE pattern is not consistent with a simple melting model, because relatively flat LREE pattern requires a relatively large degree of partial melting, in conflict with the low degree of melting required to keep residual garnet in source. Vernieres et al. (1997) used a plate model to numerically model melt–rock reaction at the transition between adiabatic and conductive mantle using a plate model. They assumed three reaction zones in which melt/rock reactions are characterized by pyroxene dissolution and olivine precipitation. The results show that melts segregated from the compaction domain display a restricted range of REE content, with REE patterns similar to that observed in Datong tholeiitic basalts (Fig. 9 in Vernieres et al., 1997).

5.4. A model for the spatial distribution of Datong basalts

The suggestion of thermo-tectonic destruction of the lithospheric root beneath the NCC (e.g., Menzies et al., 1993; Griffin et al., 1998; Xu, 2001) is now well founded. Lithospheric thinning therefore provides an appropriate geodynamic setting in which Datong tholeiitic basalts were formed by interaction of asthenospheric melts with eroded lithospheric mantle. It is widely accepted, based on many experimental and theoretical studies, that quartz tholeiites generally equilibrate at shallower depths in the mantle than alkali olivine basalts (Kushiro, 2001). Accordingly, alkali and tholeiitic basalts may sample different portions of the mantle. In this context, the isotopic compositions of Datong lavas can be interpreted as a result of mixing of the CLM (EM1) and the asthenosphere (OIB). A "plum-pudding" model, similar to that of Chung et al. (1994), is developed here to explain the spatial variation of lava types in the Datong volcanic field (Fig. 11). In this model, the reactivation of the lithospheric mantle was initiated by infiltration of small melt fractions that advectively transport heat upwards to raise the ambient temperature of the CLM. This facilitates thinning of the CLM, during which the lithosphere was gradually replaced by a "plum-pudding"-type convecting mantle

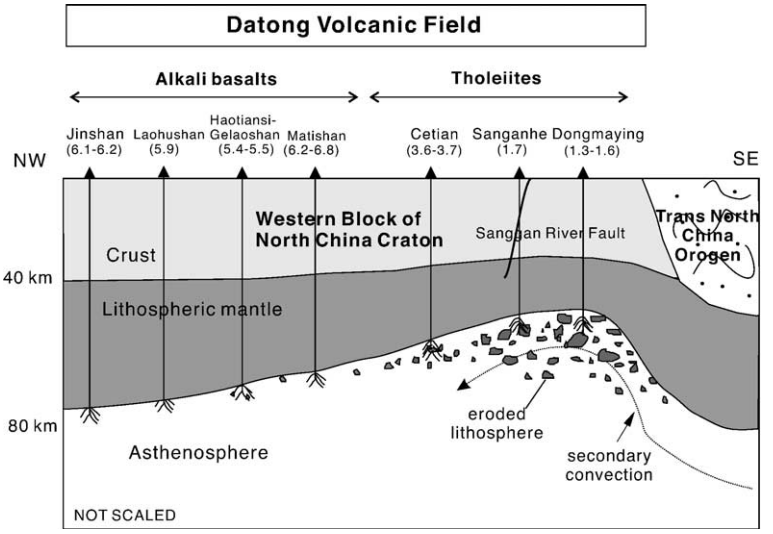

Fig. 11. Cartoon illustrating a model to account for the spatial distribution of Quaternary basalts in the Datong volcanic field. The numbers in parentheses below locality names are the ε_{Nd} range of basalts from that locality.

which assimilated materials eroded from the CLM (the "plums") with the asthenospheric materials (the "pudding"). The extent of lithospheric erosion and thinning varies as a function of lithospheric extension. The proportion of "plums" is expected to be larger in the axial region of extension than in the distal flanks (Fig. 11). As a consequence, the tholeiites, resulting from large degree of partial melting at shallower depth, involved a larger amount of eroded, enriched lithospheric mantle compared to the alkali basalts that are generated by a smaller degree of partial melting at a greater depth.

It is intriguing that tholeiitic basalts are exclusively distributed along the Sangganhe River (Fig. 1), which has long been recognized as a structural discontinuity (e.g., Zhai et al., 1996). Field observation and theoretical modeling suggest that lithospheric extension and thinning likely initiate along major structural/tectonic boundaries where the lithosphere is weakest and mantle flow becomes focused (King and Anderson, 1995). On a larger scale, Datong is located proximal to the boundary between the Western Block and Trans-North China Orogen (Fig. 1; Zhao et al., 2001). The lithosphere beneath the two blocks may be different in thickness and rheology (Ma, 1989; Zhao et al., 2001). This topographic difference may have induced secondary convection enhancing lithospheric extension along lines of weakness (King and Anderson, 1995). It is therefore conceivable that the lithospheric mantle along this zone is largely reactivated, resulting in formation of tholeiites with relatively low ε_{Nd} and high $^{87}Sr/^{86}Sr$. Mantle convection/upwelling becomes progressively weaker towards the interior of the western NC. This explains the gradual increase in ϵ_{Nd} in lavas from east to west (Fig. 11).

One tholeiitic sample (SDT-32), however, is compositionally more akin to the asthenosphere-derived alkali basalts, reflecting limited interaction with the lithospheric mantle. It is worthy noting that this sample was collected from the top of the lava succession near Sangganhe and is compositionally distinct from that (SDT-31) collected from the base of lava sequence. It is possible that such compositional variation reflects temporal decrease in the extent of lithospheric involvement in magma generation.

6. Summary and conclusion

Despite limited exposure, the Quaternary Datong volcanic field displays several distinct features that make the Datong lavas unique among the Cenozoic basalts in eastern China. In particular, the varying role of continental mantle lithosphere can be constrained using the distinct spatial distribution of alkali and tholeiitic basalt in the Datong volcanic field and the geochemical differences between Quaternary Datong basalt and the nearby but older Miocene basalt exposed ~100 km north at Hannuoba.

Alkali basalts from Datong have relatively homogenous geochemical and isotopic composition that is similar to OIB. Hence, like Hannuoba alkali basalts, they were probably derived from convecting asthenosphere. However, these alkali lava suites show contrast-

ing composition; Datong alkali basalts have lower Al_2O_3 and CaO, and higher SiO_2 and HREE contents and Na/Ti ratio than Hannuoba lavas. Such differences reflect different source composition and melting conditions. Forward modeling for Datong alkali basalts shows that a melting interval encompassing both the garnet and spinel stability fields can reconcile their relatively high Na/Ti ratios (indicative of low pressure of melting) and fractionated REE patterns that reflect residual garnet (indicative of high pressure of melting). Consequently the lithosphere was within the spinel stability field (~70 km) during generation of the Quaternary Datong volcanic field, in contrast with the relatively thick lithosphere (~100 km) associated with the formation of Miocene Hannuoba lavas. This inference, temporal thinning of the lithosphere in this region, is consistent with studies of peridotite xenoliths (Menzies et al., 1993).

The major element composition (Q-normative) of the Datong tholeiitic basalt suggests a shallow (<60 km) depth of melt segregation, but this inference conflicts with the relative REE abundances which imply control by residual garnet. This paradox, which is reminiscent of that encountered for Hawaiian tholeiites, can be reconciled if alkali basalt melts react with refractory peridotites prior to segregation from the mantle. Diagnostic geochemical consequences of this melt/rock reaction include high SiO_2 and Cr contents and "kinked" REE pattern in residual melts. This may be an important process for generation of many continental tholeiitic basalt provinces. At Datong, this melt/rock reaction most likely took place during lithospheric replacement by upwelling asthenosphere. Enhanced lithospheric extension and thinning along a major lithospheric boundary can explain the observed spatial distribution of tholeiitic and alkali basalt in the Datong volcanic field.

Acknowledgements

We thank L.B. Shi for help in the field, Y. Liu, X.L. Tu and X.R. Liang for technical assistance with diverse analyses, and Keith Putirka for his advice on Na/Ti modeling. This paper greatly benefits from numerous discussions with Dr. S. Huang and G. Xu. Financial supports from the National Science Foundation of China (49925308; 40421303) and the Chinese Academy of Sciences through a specific award to young scientist are gratefully acknowledged. Thanks are due to two anonymous referees and editor R. Rudnick for their constructive reviews. EAPS at MIT is thanked for hosting YGX's visit during which this paper was written. **[RR]**

Appendix A. Inverse modeling using rare earth elements

Because the equation for batch melting is linear (after Shaw, 1970), it is possible to measure the relative changes in the REE concentrations of erupted lavas to back-calculate source parameters. Such an inverse procedure incorporates fewer assumptions about source composition and mantle mineralogy than standard forward modeling techniques, which starts with a presumed source and then calculates the extent of melting necessary to produce the observed lavas. By assuming only that melting occurs by a batch process, the inverse technique allows the calculation of the relative changes in degree of melting of a homogeneous source, as well as some insight into the initial mantle mineralogy. The procedure has been discussed previously in some detail in Feigenson et al. (1996, 2003), and was shown to produce internally consistent results for lavas from the Hawaiian Scientific Drilling Project pilot hole (Feigenson et al., 1996), with results similar to those calculated by forward modeling of aggregated fractional melting.

The basic equation for equilibrium melting is from Shaw (1970):

$$C_l^i = \frac{C_0^i}{D_0^i + F(1 - P^i)} \tag{A1}$$

where C_l^i is the concentration of element i in the melt, C_0^i is the concentration of that element in the initial source, D_0^i is the bulk distribution coefficient of i in the source, P^i is the sum of partition coefficients of phases in the proportions that they enter the melt, and F is the degree of melting (Minster and Allègre, 1978). Albarède (1995) discusses the theoretical development of inverse modeling; the method employed here is based on modifications by Feigenson and Carr (1993). By comparing the REE to each other, the dependence of concentration on F in A1 can be eliminated, thereby reducing the number of unknown parameters from three to two. Following Minster and Allègre (1978) and Hofmann and Feigenson (1983), Eq. (A1) can be adjusted by normalizing concentrations to the initial source abundance of the most incompatible of the REE:

$$\frac{C^h}{C^i} = S^i C^h + I^i; S^i = \frac{D_o^i}{C_o^i}; I^i = \frac{C_o^h}{C_o^i}\left(1 - P^i\right) \tag{A2}$$

where C^h refers to the concentration of a highly incompatible element, S^i and I^i are the slope and intercept of the first equation, and can be evaluated from a graph of

C^h/C^i vs. C^h. This procedure removes the dependence on F and allows comparison of shapes of REE patterns; however, no explicit information on the absolute degree of melting can be obtained. The overconstraint of fixed P^i is eliminated, but the relative melt partitioning behavior is maintained, by inputting a number of different melt combinations.

We use La for C^h, as it is the most incompatible of the REE. In this way, all calculated source values for C^i and D^i can be compared relative to an assumed source concentration of La. S^i and I^i values are obtained from the "process identification diagrams" (C^h/C^i vs. C^h) of Minster and Allègre (1978). As shown by Hofmann and Feigenson (1983), source concentration and source partitioning behavior can be calculated from S^i and I^i determined from linear regressions calculated from C^h/C^i vs. C^h combined with various values of the input parameter P^i:

$$\frac{C_o^i}{C_o^{La}} = \frac{(1-P^i)}{I^i}; \frac{D_o^i}{C_o^{La}} = \frac{S^i(1-P^i)}{I^i}. \quad \text{(A3)}$$

A large range of mineral combinations are used to calculated P^i with the only restrictions that P^i must be less than one if all intercepts are positive, and that the shape of P^i must bear some resemblance to D_0^i (because the minerals that enter the melt must have been initially present in the source). This broad range of possibilities translates into the acceptable fields for source concentration and bulk partition coefficients.

References

Albarède, F., 1995. Introduction to Geochemical Modeling. Cambridge Univ. Press, New York. 543 pp.

Barry, T.L., Saunders, A.D., Kempton, P.D., Windley, B.F., Pringle, M.S., Dorjnamjaa, D., Saandar, A., 2003. Petrogenesis of Cenozoic basalts from Mongolia: evidence for the role of asthenospheric versus metasomatized lithospheric mantle sources. J. Petrol. 44, 55–91.

Basu, A.R., Wang, J.W., Huang, W.K., Xie, G.H., Tatsumoto, M., 1991. Major element, REE and Pb, Nd and Sr isotopic geochemistry of Cenozoic volcanic rocks of eastern China: implications for origin from suboceanic-type mantle reservoirs. Earth Planet. Sci. Lett. 105, 149–169.

Blundy, J.D., Falloon, T.J., Wood, B.J., Dalton, J.A., 1995. Sodium partitioning between clinopyroxene and silicate melts. J. Geophys. Res. 100, 15501–15515.

Chen, G.Y., Song, Z.H., An, C.Q., Cheng, L.H., Zhuang, Z., Fu, Z.W., Lu, Z.L., Hu, J.F., 1991. Three dimensional crust and upper mantle structure of the North China region. Acta Geophys. Sin. 34, 172–181 (in Chinese with English abstract).

Chen, W.J., Li, D.M., Dai, T.M., 1992. The K–Ar age and excess Ar of Quaternary basalt in Datong. In: Liu, R.X. (Ed.), The Age and Geochemistry of Cenozoic Volcanic Rock in China. Seismology Press, Beijing, pp. 81–92 (in Chinese).

Chen, X.D., Lin, C.Y., Zhang, X.O., 1997. Deformation features of mantle xenoliths from Quaternary basalts in Datong, Shanxi Province and their rheological implications. Seismol. Geol. 19, 314–320 (in Chinese with English abstract).

Chung, S.L., Sun, S.S., Tu, K., 1994. Late Cenozoic basaltic volcanism around the Taiwan Strait, SE China: product of lithosphere–asthenosphere interaction during continental extension. Chem. Geol. 112, 1–20.

Cox, K.G., 1980. A model for flood basalt volcanism. J. Petrol. 21, 629–650.

Cox, K.G., Hawkesworth, C.J., 1984. Relative contribution of crust and mantle to flood basalt magmatism, Mahabaleshwar area, Deccan Traps. Philos. Trans. R. Soc. Lond., A 310, 627–641.

DePaolo, D.J., 1981. Trace element and isotopic effects of combined wallrock assimilation and fractional crystallization. Earth Planet. Sci. Lett. 53, 189–202.

DePaolo, D.J., Daley, E.E., 2000. Neodymium isotopes in basalts of the southwest basin and range and lithospheric thinning during continental extension. Chem. Geol. 169, 157–185.

Eggins, S.M., 1992a. Petrogenesis of Hawaiian tholeiites: 1. Phase equilibria constraints. Contrib. Mineral. Petrol. 110, 387–397.

Eggins, S.M., 1992b. Petrogenesis of Hawaiian tholeiites: 2. Aspects of dynamic melt segregation. Contrib. Mineral. Petrol. 110, 387–397.

Fan, Q., Hooper, P.R., 1991. The Cenozoic basaltic rocks of eastern China: petrology and chemical composition. J. Petrol. 32, 765–810.

Fan, Q.C., Chen, W.J., Hurford, A.J., et al., 1992. The major and trace element chemistry of Quaternary basalt in Datong. In: Liu, R.X. (Ed.), The Age and Geochemistry of Cenozoic Volcanic Rock in China. Seismology Press, Beijing, pp. 93–100 (in Chinese).

Fan, W.M., Zhang, H.F., Baker, J., Javis, K.E., Mason, P.R.D., Menzies, M.A., 2000. On and off the North China craton: where is the Archaean keel? J. Petrol. 41, 933–950.

Feigenson, M.D., Carr, M.J., 1993. The source of Central American lavas: inferences from geochemical inverse modeling. Contrib. Mineral. Petrol. 113, 226–235.

Feigenson, M.D., Patino, L.C., Carr, M.J., 1996. Constraints on partial melting imposed by rare earth element variations in Mauna Kea basalts. J. Geophys. Res. 101 (B5), 11815–11829.

Feigenson, M.D., Bolge, L.L., Carr, M.J., Herzberg, C.T., 2003. REE inverse modeling of HSDP2 basalts: evidence for multiple sources in the Hawaiian plume. Geochem. Geophys. Geosyst. 4. doi:10.1029/2001GC000271.

Fitton, J.G., James, D., Leeman, W.P., 1991. Basic magmatism associated with Late Cenozoic extension in the western United States: compositional variation in space and time. J. Geophys. Res. 96, 13693–13711.

Fram, M.S., Lesher, C.F., 1993. Geochemical constraints on mantle melting during creation of the North Atlantic basin. Nature 363, 712–715.

Frey, F.A., Green, D.H., Roy, S.D., 1978. Integrated models of basalt petrogenesis: a study of quartz tholeiites to olivine melilitites from southeastern Australia utilizing geochemical and experimental petrological data. J. Petrol. 19, 463–513.

Frey, F.A., Garcia, M.O., Roden, M.F., 1994. Geochemical characteristics of Koolau volcano: implications of intershield geochemical differences among Hawaiian volcanoes. Geochim. Cosmochim. Acta 58, 1141–1162.

Gao, S., Rudnick, R.L., Carlson, R.W., McDonough, W.F., Liu, Y.S., 2002. Re–Os evidence for replacement of ancient mantle litho-

sphere beneath the North China Craton. Earth Planet. Sci. Lett. 198, 307–322.

Glazner, A., Farmer, G.L., 1992. Production of isotopic variability in continental basalts by cryptic crustal contamination. Science 255, 72–74.

Godard, M., Bodinier, J.-L., Vasseur, G., 1995. Effects of mineralogical reaction on trace element redistributions in mantle rocks during percolation processes: a chromatographic approach. Earth Planet. Sci. Lett. 133, 449–461.

Goto, A., Tatsumi, Y., 1996. Quantitative analyses of rock samples by an X-ray fluorescence spectrometer (II). Rigaku J. 13, 20–39.

Govindaraju, K., 1989. Compilation of working values and sample description data for 272 geostandards. Geostand. Newsl. 13, 1–114.

Griffin, W.L., Zhang, A.D., O'Reilly, S.Y., Ryan, G., 1998. Phanerozoic evolution of the lithosphere beneath the Sino–Korean Craton. In: Flower, M., Chung, S.L., Lo, C.H., Lee, T.Y. (Eds.), Mantle Dynamics and Plate Interactions in East Asia, Am. Geophys. Union. Geodynamic Series, vol. 27, pp. 107–126.

Hauri, E., 1996. Major-element variability in the Hawaiian mantle plume. Nature 382, 415–419.

Hirschmann, M.M., Stopler, E.M., 1996. A possible role for garnet pyroxenite in the origin of the "garnet signature" in MORB. Contrib. Mineral. Petrol. 124, 185–208.

Hofmann, A.W., 1988. Chemical differentiation of the earth: the relationship between mantle continental crust and oceanic crust. Earth Planet. Sci. Lett. 79, 270–280.

Hofmann, A.W., Feigenson, M.D., 1983. Feigenson, case studies on the origin of basalt: I. Theory and reassessment of Grenada basalts. Contrib. Mineral. Petrol. 84, 382–389.

Hofmann, A.W., Jochum, K.P., Seufert, M., White, W.M., 1986. Nb and Pb in oceanic basalts: new constraints on mantle evolution. Earth Planet. Sci. Lett. 79, 33–45.

Johnson, K.T.M., 1998. Experimental determination of partition coefficients for rare earth and high-field-strength elements between clinopyroxene, garnet and basaltic melt at high pressures. Contrib. Mineral. Petrol. 133, 60–68.

Johnson, K.T.M., Dick, H.J.B., Shimizu, N., 1990. Melting in the oceanic upper mantle: an ion microprobe study of diopsides in abyssal peridotites. J. Geophys. Res. 95, 2661–2678.

Jung, S., Masberg, P., 1998. Major- and trace-element systematics and isotopic geochemistry of Cenozoic mafic volcanic rocks from the Vogelsberg (central Germany): constraints on the origin of continental alkaline and tholeiitic basalts and their mantle sources. J. Volcanol. Geotherm. Res. 86, 151–177.

Kushiro, I., 2001. Partial melting experiments on peridotite and origin of mid-ocean ridge basalt. Annu. Rev. Earth Planet. Sci. 29, 71–107.

Kelemen, P.B., Dick, H.J.B., Quick, J.E., 1992. Formation of harzburgite by pervasive melt/rock reaction in the upper mantle. Nature 358, 635–640.

King, S.D., Anderson, D.L., 1995. An alternative mechanism of flood basalt formation. Earth Planet. Sci. Lett. 136, 269–279.

Kinzler, R.J., 1997. Melting of mantle peridotite at pressure approaching the spinel to garnet transition: application to mid-ocean ridge petrogenesis. J. Geophys. Res. 102, 853–874.

Klemme, S., O'Neill, H. StC., 2000. The near-solidus transition from garnet to spinel lherzolite. Contrib. Mineral. Petrol. 138, 237–248.

Langmuir, C.H., Klein, E.M., Plank, T., 1992. Petrological systematics of mid-ocean ridge basalts: constraints on melt generation beneath ocean ridges. In: Morgan, J.P., Blackman, D.K., Sinton, J.M. (Eds.), Mantle Flow and Melt Generation at Mid-Ocean Ridges, Geophys Monogr Series, vol. 71. AGU (American Geophysic Union), Washington DC, pp. 81–180.

Le Bas, M., Le Maitre, R.W., Strekeisen, A., Zanettin, B., 1986. A chemical classification of volcanic rocks based on the total alkali–silica diagram. J. Petrol. 27, 745–750.

Liu, R.X., Chen, W.J., Sun, J.Z., Li, D.M., 1992. The K–Ar age and tectonic environment of Cenozoic volcanic rock in China. In: Liu, R.X. (Ed.), The Age and Geochemistry of Cenozoic Volcanic Rock in China. Seismologic Press, Beijing, pp. 1–43 (in Chinese).

Liu, C.Q., Masuda, A., Xie, G.H., 1994. Major- and trace-element compositions of Cenozoic basalts in eastern China: petrogenesis and mantle source. Chem. Geol. 114, 19–42.

Ma, X. (Ed.), 1989. Atlas of Active Faults in China. Seismological press, Beijing. 120 pp.

McDonald, G.A., Katsura, T., 1964. Chemical composition of Hawaiian Lavas. J. Petrol. 5, 82–133.

McKenzie, D.P., O'Nions, R.K., 1991. Partial melt distributions from inversion of rare earth element concentrations. J. Petrol. 32, 1021–1091.

Menzies, M.A., Xu, Y.G., 1998. Geodynamics of the North China Craton. In: Flower, M., Chung, S.L., Lo, C.H., Lee, T.Y. (Eds.), Mantle Dynamics and Plate Interactions in East Asia, Am. Geophys. Union. Geody. Series, vol. 27, pp. 155–165.

Menzies, M.A., Fan, W.M., Zhang, M., 1993. Palaeozoic and Cenozoic lithoprobes and the loss of >120 km of Archaean lithosphere, Sino–Korean craton, China. In: Prichard, H.M., Alabaster, T., Harris, N.B.W., Neary, V.R. (Eds.), Magmatic Processes and Plate Tectonics, Geol. Soc. Spel. Pub., vol. 76, pp. 71–78.

Minster, J.F., Allègre, C.J., 1978. Systematic use of trace elements in igneous processes: III. Inverse problem of batch partial melting in volcanic suites. Contrib. Mineral. Petrol. 68, 37–52.

O'Neill, H.S.C., 1981. The transition between spinel lherzolite and garnet lherzolite, and its use as a geobarometer. Contrib. Mineral. Petrol. 77, 185–194.

Peng, Z.C., Zartman, R.E., Futa, E., Chen, D.G., 1986. Pb-, Sr- and Nd-isotopic systematics and chemical characteristics of Cenozoic basalts, eastern China. Chem. Geol. 59, 3–33.

Perry, F.V., Baldridage, W.S., DePaolo, D.J., 1987. Role of asthenosphere and lithosphere in the genesis of Late Cenozoic basaltic rocks from the Rio Grande rift and adjacent regions of the southwestern United States. J. Geophys. Res. 92, 9193–9213.

Putirka, K., 1999a. Melting depth and mantle heterogeneity beneath Hawaii and the East Pacific Rise: constraints from Na/Ti and rare earth element ratios. J. Geophy. Res. 104, 2817–2829.

Putirka, K., 1999b. Clinopyroxene+liquid equilibria to 100 kbar and 2450 K. Contrib Mineral. Petrol. 135, 151–163.

Rampone, E., Romairone, A., Hofmann, A.W., 2004. Contrasting bulk and mineral chemistry in depleted mantle peridotites: evidence for reactive porous flow. Earth Planet. Sci. Lett. 218, 491–506.

Ren, J., Tamaki, K., Li, S., Zhang, J., 2002. Late Mesozoic and Cenozoic rifting and its dynamic setting in eastern China and adjacent areas. Tectonophysics 344, 175–205.

Robinson, J.A., Wood, B.J., 1998. The depth of the spinel to garnet transition at the peridotite solidus. Earth Planet. Sci. Lett. 164, 277–284.

Rudnick, R.L., Gao, S., Ling, W-l., Liu, Y.S., McDonough, W.F., 2004. Petrology and geochemistry of spinel peridotite xenoliths from Hannuoba and Qixia, North China craton. Lithos 77, 609–637.

Shaw, D.M., 1970. Trace element fractionation during anatexis. Geochim. Cosmochim. Acta 34, 237–243.

Song, Y., Frey, F.A., 1989. Geochemistry of peridotite xenoliths in basalt from Hannuoba, eastern China: implications for subcontinental mantle heterogeneity. Geochim. Cosmochim. Acta 53, 97–113.

Song, Y., Frey, F.A., Zhi, X., 1990. Isotopic characteristics of Hannuoba basalts, eastern China: implications for their petrogenesis and the composition of subcontinental mantle. Chem. Geol. 88, 35–52.

Sun, S.-S., McDonough, W.F., 1989. Chemical and isotopic systematics of oceanic basalts: implications for mantle composition and processes. In: Saunders, A.D., Norry, M.J. (Eds.), Magmatism in the Ocean Basins, Geol. Soc. Spel. Pub., vol. 42, pp. 313–345.

Takahashi, E., Kushiro, I., 1983. Melting of a dry peridotite at high pressures and basalt magma genesis. Am. Mineral. 68, 859–879.

Tanaka, T., Togashi, S., Kamioka, H., et al., 2004. JNdi-1: a neodymium isotopic reference in consistency with LaJolla neodymium. Chem. Geol. 168, 279–281.

Tatsumoto, M., Basu, A.R., Huang, W.K., Wang, J.W., Xie, G.H., 1992. Sr, Nd, and Pb isotopes of ultramafic xenoliths in volcanic rocks of eastern China: enriched components EMI and EMII in subcontinental lithosphere. Earth Planet. Sci. Lett. 113, 107–128.

Taylor, S.R., McLennan, S.M., 1985. The Continental Crust: Its Composition and Evolution. Blackwell Scientific Publication, pp. 209–230.

Van der Wal, D., Bodinier, J.-L., 1996. Origin of the recrystallisation front in the Ronda peridotite by km-scale pervasive porous melts flow. Contrib. Mineral. Petrol. 122, 387–405.

Vernieres, J., Godard, M., Bodinier, J.-L., 1997. A plate model for the simulation of trace element fractionation during partial melting and magmas transport in the Earth's upper mantle. J. Geophys. Res. 102, 24771–24784.

Wagner, T.P., Grove, T.L., 1998. Melt/harzburgite reaction in the petrogenesis of tholeiitic magma from Kilauean volcano, Hawaii. Contrib. Mineral. Petrol. 131, 1–12.

Walter, M.J., 1998. Melting of garnet peridotite and the origin of komatiite and depleted lithosphere. J. Petrol. 39, 29–60.

Weaver, B.L., 1991. The origin of ocean island basalt end-member composition: trace element and isotopic constraints. Earth Planet. Sci Lett. 104, 381–397.

Wilson, M., Downes, H., 1991. Tertiary–Quaternary extension-related alkali magmatism in western and central Europe. J. Petrol. 32, 811–849.

Wu, Y.S., Wang, X.W., 1978. Recent basalts in Shanxi Province. Team of Regional Geology Survey of the Geology Bureau of Shanxi Province, pp. 1–136 (in Chinese).

Wu, F.Y., Lin, J.Q., Wilde, S.A., Zhang, X., Yang, J.H., 2005. Nature and significance of the Early Cretaceous giant igneous event in eastern China. Earth Planet. Sci Lett. 233, 103–119.

Xu, Y.-G., 2001. Thermo-tectonic destruction of the Archaean lithospheric keel beneath eastern China: evidence, timing and mechanism. Phys. Chem. Earth, Part A Solid Earth Geod. 26, 747–757.

Xu, Y.-G., 2002. Evidence for crustal components in the mantle and constraints on crustal recycling mechanisms: pyroxenite xenoliths from Hannuoba, North China. Chem. Geol. 182, 301–322.

Xu, Y.G., Menzies, M.A., Mattey, D.P., Lowry, D., Harte, B., Hinton, R.W., 1996. The nature of the lithospheric mantle near the Tancheng–Lujiang fault, China: an integration of texture, chemistry and O isotopes. Chem. Geol. 134, 67–82.

Xu, Y.G., Menzies, M.A., Vroon, P., Mercier, J.C.C., Lin, C.Y., 1998. Texture–temperature–geochemistry relationship in the upper mantle as revealed from spinel peridotite xenoliths from Wangqing, NE China. J. Petrol. 39, 469–493.

Xu, Y.G., Menzies, M.A., Thirlwall, M.F., Huang, X.L., Liu, Y., Chen, X.M., 2003. "Reactive" harzburgites from Huinan, NE China: products of the lithosphere–asthenosphere interaction during lithospheric thinning? Geochim. Cosmochim. Acta 67, 487–505.

Xu, Y.-G., Chung, S.-L., Ma, J., Shi, L., 2004a. Contrasting Cenozoic lithospheric evolution and architecture in western and eastern Sino–Korean Craton: constraints from geochemistry of basalts and mantle xenoliths. J. Geol. 112, 593–605.

Xu, Y.-G., Huang, X.L., Ma, J.L., Wang, Y.B., Iizuka, Y., Xu, J.F., Wang, Q., Wu, X.Y., 2004b. Crustal–mantle interaction during the thermo-tectonic reactivation of the North China Craton: SHRIMP zircon U–Pb age, petrology and geochemistry of Mesozoic plutons in western Shandong. Contrib. Mineral. Petrol. 147, 750–767.

Ye, H., Zhang, B., Mao, F., 1987. The Cenozoic tectonic evolution of the Great North China: two types of rifting and crustal necking in the Great North China and their tectonic implications. Tectonophysics 133, 217–227.

Zhai, M.G., Guo, J.H., Yan, Y.H., Li, Y.G., Li, J.H., Zhang, W.H., 1996. An oblique cross-section of Archaean continental crust in Shanxi–Hebei–Nei Mongol juncture area, North China Craton. Acta Petrol. Sin. 12, 222–238 (in Chinese with English abstract).

Zhao, G.C., Wilde, S.A., Cawood, P.A., Sun, M., 2001. Archean blocks and their boundaries in the North China Craton: lithological, geochemical, structural and *P*–*T* path constraints and tectonic evolution. Precambrian Res. 107, 45–73.

Zheng, J.P., O'Reilly, S.Y., Griffin, W.L., et al., 1998. Nature and evolution of Cenozoic lithospheric mantle beneath Shandong peninsula, Sino–Korean craton, eastern China. Int. Geol. Rev. 40, 471–499.

Zhi, X., Song, Y., Frey, F.A., Feng, J., Zhai, M., 1990. Geochemistry of Hannouba basalts, eastern China: constraints on the origin of continental alkali and tholeiitic basalt. Chem. Geol. 88, 1–33.

Zhou, X.H., Armstrong, R.L., 1982. Cenozoic volcanic rocks of eastern China— secular and geographic trends in chemistry and strontium isotopic composition. Earth Planet. Sci. Lett. 59, 301–329.

Zhou, P.B., Mukasa, S.B., 1997. Nd–Sr–Pb isotopic, and major- and trace element geochemistry of Cenozoic lavas from the Khorat Plateau, Thailand: source and petrogenesis. Chem. Geol. 137, 175–193.

Zindler, A., Hart, S.R., 1986. Chemical geodynamics. Annu. Rev. Earth Planet. Sci. 14, 493–571.

Zou, H.B., Zindler, A., Xu, X.S., Qu, Q., 2000. Major, trace element, and Nd, Sr and Pb isotopic studies of Cenozoic basalts in SE China: mantle sources, regional variations, and tectonic significance. Chem. Geol. 171, 35–47.